

An improved understanding of the roles of atomic processes and power balance in divertor target ion current loss during detachment

K. Verhaegh^{1,2}, B. Lipschultz¹, B.P. Duval², O. Février², A. Fil^{1,3}, C. Theiler², M. Wensing², C. Bowman^{1,3}, D.S. Gahle^{4,3}, J.R. Harrison³, B. Labit², C. Marini², R. Maurizio², H. de Oliveira², H. Reimerdes², U. Sheikh², C.K. Tsui^{5,2}, N. Vianello⁶, W.A.J. Vijvers⁷, the TCV team⁸ and the EUROfusion MST1 team⁹

¹ York Plasma Institute, University of York, United Kingdom

² Ecole Polytechnique Fédérale de Lausanne (EPFL), Swiss Plasma Center (SPC), CH-1015 Lausanne, Switzerland

³ Culham Centre for Fusion Energy, Culham Science Centre, OX14 3DB, UK

⁴ Department of Physics SUPA, University of Strathclyde, Glasgow, G4 0NG, UK

⁵ University of California San Diego (UCSD), San Diego, United States

⁶ Consorzio RFX, Padova, Italy

⁷ DIFFER, Eindhoven, The Netherlands

⁸ See the author list of S. Coda et al. 2017 Nucl. Fusion 57 102011

⁹ See the author list of H. Meyer et al. 2017 Nucl. Fusion 57 102014

Abstract

The process of divertor detachment, whereby heat and particle fluxes to divertor surfaces are strongly reduced, is required to reduce heat loading and erosion in a magnetic fusion reactor. In this paper the physics leading to the decrease of the total divertor ion current (I_t), or ‘roll-over’, is experimentally explored on the TCV tokamak through characterization of the location, magnitude and role of the various divertor ion sinks and sources including a complete measure of particle and power balance. These first measurements of the profiles of divertor ionisation and hydrogenic radiation along the divertor leg are enabled through novel spectroscopic techniques which are introduced.

Over a range in TCV plasma conditions (different levels of plasma current and electron density, with/without impurity-seeding) the I_t roll-over is due to a drop in the divertor ion source; recombination remains either small or negligible until later in the detachment process. The ion source reduction is driven by both a reduction in the power available for ionization, P_{recl} , and concurrent increase in the energy required per ionisation, E_{ion} : sometimes characterised as ‘power starvation’. The detachment threshold is found experimentally (in agreement with analytic model predictions) to be $\sim P_{\text{recl}}/I_t E_{\text{ion}} \sim 2$, which corresponds to the target electron temperature, $T_t \sim E_{\text{ion}}/\gamma$ where γ is the sheath transmission coefficient. The loss in target pressure, required for target ion current loss, is driven not by just volumetric momentum loss as typically assumed but also due to a drop of upstream pressure.

The measured evolution through detachment of the divertor profile of various ion sources/sinks as well as power losses, charge exchange and molecular/atomic components of the Da emission are quantitatively reproduced through full 2D SOLPS modelling of a ramp of core plasma density through the detachment process.

1. Introduction

Divertor detachment is predicted to be of paramount importance in handling the power exhaust of future fusion devices such as ITER [1]. Aside from target power deposition due to radiation and

neutrals, the plasma heat flux (q_t in W/m^2) is dependent on the divertor target ion flux density (Γ_t in $ions/m^2$) and electron temperature (T_t in eV):

$$q_t = \Gamma_t(\gamma T_t + \epsilon) \quad (1)$$

where γ is the sheath transmission coefficient ($\gamma \sim 7$) and ϵ is the potential energy deposited on the target (13.6 eV for deuterium ion recombination into an atom), with the kinetic energy deposited being $\Gamma_t \gamma T_t$. Here, the energy released by recombination into molecules (~ 2.2 eV dissociation potential [1, 2]) is ignored and we use ‘kinetic’ to mean ‘kinetic and thermal’. Detachment provides the reduction of target heat flux by reducing both T_t and Γ_t lowering both the potential and kinetic contributions. The processes involved were identified early on as including particle, energy and momentum loss [3-7]. Equation 2 serves as the basis for discussion of the required drop in Γ_t :

$$\Gamma_t \propto n_t C_s \propto p_t / T_t^{1/2} \quad (2)$$

where C_s , T_t and p_t are the target ion sound speed, temperature and pressure respectively assuming a target Mach number of 1.

Detachment is preceded by the heat flux along the field being conduction limited, which allows a temperature (density) gradient to form along the field lines *while the total pressure remains roughly constant*. Therefore, as the target temperature drops for such attached conditions (p_t constant) – both due to conduction and radiative dissipation, lowering the kinetic heat flow reaching the target - there is a strong rise in Γ_t (Equation 2). Although the kinetic energy deposited at the target is dropping proportional to $T_t^{1/2}$, the potential energy reaching the target rises, proportional to $1/T_t^{1/2}$. Radiative dissipation and heat conduction thus cannot simultaneously reduce T_t and Γ_t , required to lower both the thermal energy deposited at the target ($\Gamma_t \gamma T_t$) and the potential energy reaching the target ($\Gamma_t \epsilon$).

Detachment can achieve this goal through a simultaneous reduction of T_t and Γ_t which is inextricably linked to a reduction of target pressure, Equation 2. In fact, p_t must drop faster than $T_t^{1/2}$ for Γ_t to drop. Note that the drop in p_t does not necessitate any momentum loss along the field lines, although we would not consider a case without any volumetric pressure loss in the flux tube to be detachment. In the absence of momentum losses, the upstream pressure, p_u , would need to drop during the ion current roll-over. One could imagine, for instance, a case where the upstream pressure is constant along a flux tube, but due to changes in the core plasma the pressure all along the flux tube is reduced. Such a degradation of the upstream pressure can influence the core plasma [4] and is thus to be avoided for a reactor-relevant divertor solution. This requires $p_u \gg p_t$ and thus necessitates volumetric momentum loss to reduce p_t . A degradation of the upstream pressure along with volumetric momentum loss is observed during TCV detachment in this work, as well as during recent COMPASS detachment experiments [8].

Target-current rollover is often taken to be the definition of detachment (although sometimes it is simply defined as T_t being less than some specified value, e.g. [9]). Therefore, in addition to playing a central role in the control of target heat flux, Γ_t (or the integrated Γ_t along the divertor target, which is I_t in ion/s) is experimentally important as a marker for the occurrence of detachment, it is the most accurately and easily measured detachment indicator in most tokamaks (using Langmuir probes) compared to others like p_t and T_t . However, one must still be careful in using the behaviour of I_t as a measure of detachment given the role the upstream pressure can play). Experimentally studying the role of the various processes of momentum, power and particle loss leading to the drop in Γ_t during detachment is thus an important area of research. More detailed information from experiments will provide a better basis for (in)validation of our current models of divertor plasma characteristics.

The loss of Γ_t during detachment is often described from a viewpoint that emphasises pressure drop along the field lines [3, 4, 9]. Assuming a fixed p_u , such a pressure drop can be correlated with a Γ_t reduction eqn. (2). Pressure drop is usually attributed to the dominance of ion-neutral reactions (e.g. charge exchange and ion-molecule) over ionisation reactions at low temperatures ($T_e \lesssim 5\text{-}10\text{ eV}$ [4, 9]). Such studies note that the simultaneous reduction of Γ_t and T_t requires both parallel power loss as well as pressure loss.

Some researchers have also described the loss of Γ_t from a viewpoint that emphasises power and particle balance [7, 10-13]. In such models the divertor region is assumed to be ‘self-contained’ in the sense that the target ion flux is dominated by the sum of ion sources in the divertor (ionisation) minus the sum of ion sinks (recombination) [7, 10, 11]. We define this as high recycling conditions [10, 14]. This simplification ignores the ion flux into the divertor from upstream along a flux tube and any cross-field transport of particles (and momentum). Both the decrease in divertor ion source and increase in ion sink can play an important role. Those studies maintain that momentum loss, for instance through ion-neutral collisions, does not directly lead to a loss of Γ_t [10-12] but is a consequence of a reduction in power flow to the target lowering T_t and creating the conditions for momentum loss.

While viewing target ion current roll-over during detachment alternatively through the viewpoints of pressure loss or as a competition between ion sources (ionisation) and sinks (recombination) may appear to describe detachment differently, they are, in fact, not mutually exclusive and all cited processes can/will occur [4, 9, 10]. In this paper we show that both power loss (in fact power-limitation of the ion source) and volumetric momentum loss are both required to describe the TCV detachment observations.

Volumetric recombination is generally predicted to play a central role in target ion flux reduction [15-20]. The existence of volumetric recombination has been confirmed experimentally [7, 21-25] and is sometimes found, through quantitative analysis, to be significant in the reduction of the ion target flux [7, 22-26]. However, in previous work on TCV [27], the volumetric recombination rate was shown to be only a small fraction of the reduction of ion flux, which is in agreement with recent TCV simulations [28], but in contrast with earlier TCV simulations [20]. Earlier studies of detachment in C-Mod [7, 23, 26] and ASDEX-Upgrade [24] (both higher density than TCV) show a range of contributions of recombination to target ion current loss from important to small (e.g. N_2 -seeded discharges in C-Mod [6]).

The ion target flux Γ_t , which in steady-state equals the ionization rate (Γ_i) if recombination is negligible, must be compatible/consistent with the power entering the recycling region, the power used in the ionisation process and the power reaching the target. Each ionization in the recycling region ‘costs’ a certain amount of energy per ionisation, which we define as E_{ion} , which is comprised of two parts: a) the 13.6 eV (ε of Equation 1) required to take a bound electron to the continuum, and b) the amount of energy radiated arising from excitation collisions preceding ionisation. The power flux entering the recycling region (here termed q_{recl}) supplies that ionization cost ($\Gamma_t E_{ion}$), and thus Γ_t , as well as the power corresponding to the kinetic and thermal energy of the plasma arriving at the target, $\Gamma_t \gamma T_{e,t}$. Using power balance (in the absence of recombination), Equation 3 must then hold [7, 10, 11, 14, 18]. Note that q_{recl} is larger than what reaches the target (Equation 1) due to excitation energy loss in E_{ion} . Therefore, as an alternative to reducing Γ_t through volumetric recombination, the ion source in the divertor itself can be reduced through a lack of sufficient power flowing into the ionisation region: a form of ‘power limitation’ (sometimes referred to as ‘power starvation’ [10, 14]).

$$\Gamma_t = \frac{q_{recl}}{E_{ion} + \gamma T_t} \quad (3)$$

Such power limitation has been quantitatively identified in experiments [7] and SOLPS simulations [11, 29, 30] as well as simple model predictions [7, 10, 11, 14, 18]. Such a reduction of Γ_t also requires target pressure loss (Equation 2), which requires either an upstream pressure drop, volumetric momentum losses or a mix. References [4,8] show more explicitly that in the case that p_u is held constant (volumetric) momentum-pressure loss, which becomes increasingly stronger at lower temperatures, (Figure 24 of [8]) is required for the target ion current to drop. A reduction in the q_{recl} could be realised through either increasing impurity radiation *inside* the divertor (shown in this paper) or by reducing the power flowing into the SOL [31]. Power limiting the ion source can be as important as recombination in target ion current loss, if not the primary process [7, 10, 11, 29]. Although experimental indications for such a process are available (either from inferred ion sources [7], or from qualitative spectroscopic ‘indicators’ based on D_α [32]), one weakness of previous results is that this hypothesized reduction of the ion source during detachment has not been measured quantitatively. However, recent studies aim to provide quantitative information on ionisation during divertor detachment [33, 34].

Our techniques for achieving this are described in [35], which enables directly estimating a) the ionization source/recombination sink and their profiles throughout the outer divertor leg; and b) the total energy ‘cost’ per ionization, E_{ion} per ionisation event. This information is shown in section 3 and is compared with reduced analytical models [4, 7, 9, 10, 18], accounting for a minimum number of physical processes necessary to describe the observed detachment dynamics (section 4). Assuming knowledge of the target temperature, one only needs to consider power and particle balance to predict the target ion flux rollover (Eq 3). However, including momentum balance is necessary to predict T_t (and thus the magnitude and trend in the target ion current) while molecular reactions need to be included to explain our D_α observations as shown in [36].

Our results (section 3) quantitatively verify that, at least for the TCV cases shown, the loss of target ion current is primarily due to an ionization source loss. Recombination, as an ion sink, has a smaller effect. This loss of ion source coincides with the power entering the recycling region (P_{recl}) approaching the power required for ionisation (P_{ion}). The experimentally-determined profiles of ionization, recombination, electron density, impurity radiation along the divertor leg together with their variation in time are compared with SOLPS and show both qualitative and quantitative agreement.

We have found experimentally that the detachment process starts when $P_{recl} \sim 2 P_{ion}$ with a flattening of the integrated ion target current as the upstream density is increased, at which point the target temperature is measured (using spectroscopic estimates) to be $\sim 4-6$ eV. Those empirical, experimental ‘detachment thresholds’ are consistent with detachment thresholds predicted by analytic models [10, 14]. Combining power/particle balance (eq 3) with the Bohm sheath criterion (eq 2), leads to an analytic model prediction for the onset of target pressure loss when power limitation limits the rise in I_t as function of T_t such that p_t has to drop (eq 2); this corresponds to $P_{recl} = 2 P_{ion}$, $T_t = E_{ion}/\gamma$ as a well as a critical threshold for the ratio between the upstream pressure (assuming pressure balance) and the heat flux entering the recycling region: p_u/q_{recl} . Quantitative agreement is found between the measured and predicted onset of detachment for all three criteria available to compare with data.

The picture that emerges from our TCV studies is that power limitation starts the detachment process through stopping/slowing the linear growth in TCV target ion current with upstream density predicted using a Two-point Model [4] which includes recycling energy losses (appendix A.4). At the same time T_t accesses a temperature range conveniently conducive to momentum loss ($T_t < E_{ion}/\gamma$) which slows the rise in I_t as a function of T_t (Equation 2) and leads to target current roll-over as p_t drops faster than

T_t . Power limitation dominates the loss of ion source throughout the detached (I_t roll-over) phase. As P_{recl} continues to approach P_{ion} after roll-over the target temperature reaches values conducive to recombination, resulting in a strong rise of the recombination rate. We feel that the above picture is applicable to various approaches to detachment – density scans, P_{SOL} reductions and impurity seeding. It also applies to higher density experiments where the effect of recombination, while larger than for TCV, must still await the drop in the T_t to low enough values driven by power limitation.

2. Experimental setup

All the research discussed involved L-mode Ohmic density/impurity ramp discharges made in the medium-sized tokamak, TCV ($R = 0.89$ m, $a = 0.25$ m, $B_t = 1.4$ T)[37]. The characteristics of the various discharges utilised, as well as their equilibria, are shown in table 1 and Figure 1a, respectively.

To obtain ionisation sources and sinks, we utilised the newly developed TCV divertor spectroscopy

Discharge number	I_p (kA)	Greenwald fraction	
56567 (and repeats)	340	0.3 – 0.6	Density ramp
54868	240	0.25 – 0.6	Density ramp
52158	340	0.4	N_2 seeding ramp
57912	340	0.25 – 0.6	Density ramp

Table 1: Overview of discharges used in this work, together with their shot numbers, plasma current and Greenwald fraction.

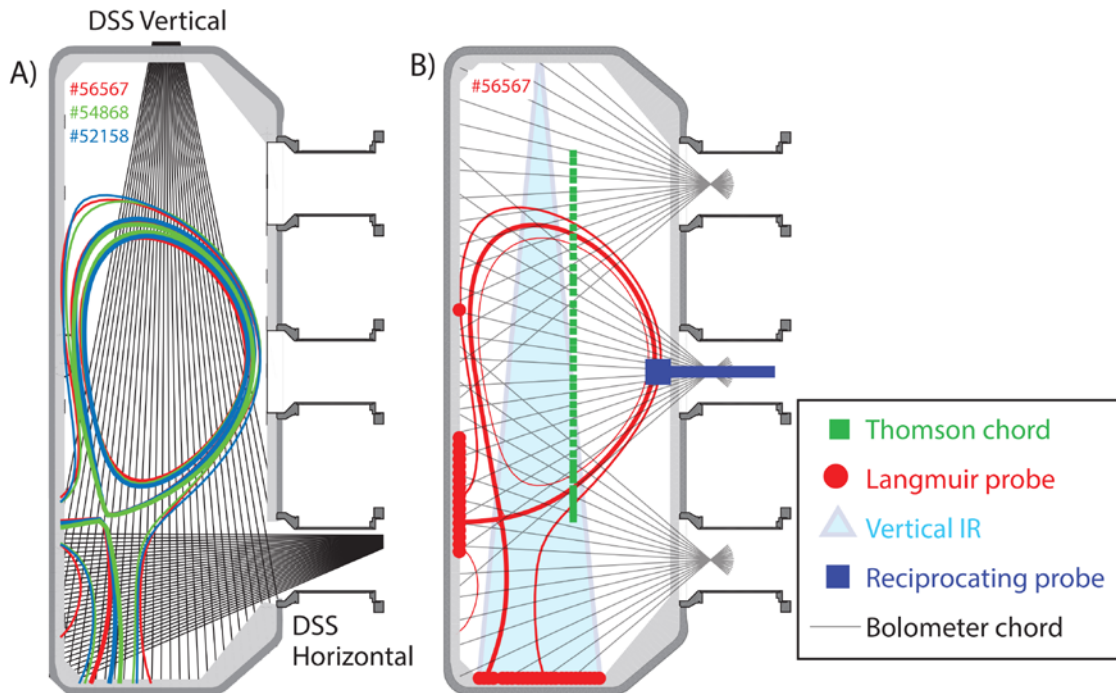


Figure 1. a): Lines of sight of the horizontal and vertical DSS systems. Divertor geometries for #56567 (red), #54868 (green), #52158 (blue) are shown. b) Lines of sight and locations of other diagnostics (Thomson/Langmuir probes/Vertical IR/Reciprocating probe/Bolometry together with the divertor geometry of #56567.

system (DSS) [27, 35, 36]. The DSS consists of vertical and horizontal viewing systems, each employing 32 lines of sight (Figure 1a). Our analysis is based on the horizontal system, which provides full coverage for the divertor shapes studied in this work. Full details on the analysis can be found in [35, 36] and a summary can be found in section 2.1.

Other diagnostics used for portions of the work presented are gold foil bolometers, target Langmuir probes [38], an upgraded Thomson scattering system [39], a reciprocating probe [40] and infrared imaging [41]. The locations of these different diagnostics are shown in Figure 1b.

We have divided the radiated power into core radiation (above the x-point) and divertor radiation (below the x-point). This is accomplished by utilising the brightness from poloidal bolometric chords over the appropriate region, while removing chords which intersect the inner divertor (to prevent contamination from inner divertor radiation). Such an analysis of bolometric chordal brightnesses has been used in place of the tomographic reconstruction of the radiated power emissivity across the entire plasma which can have significant uncertainties [42]. We note that due to the reflection of low energy photons from the gold foil of the bolometers, the estimated radiated power is assumed to be underestimated by at least 15% [43]. When considering other uncertainties, the overall underestimate of the radiated power ranges from 10% - 20%, which we correct for in our power balance analysis. Further explanation on the bolometric analysis can be found in [36].

2.1 Spectroscopic analysis methodology

We first provide a brief summary of our analysis techniques (a more detailed description can be found in [35]) and nomenclature for inferring the recombination sink [27], ionisation source and hydrogenic power loss. Figure 2 illustrates the various steps in the analysis process, eventually resulting in estimates of both local plasma characteristics (weighted over the Balmer line emission profile along each viewing chord) and line integrated plasma parameters. After the Balmer line shape is analysed to obtain a (Stark) density estimate, the analysis starts with the Balmer line ratio – which allows the determination of the fraction of the Balmer line brightness due to recombination, $F_{rec}(n)$, and excitation, $F_{exc}(n)$, to separate the excitation/recombination contributions of the Balmer line

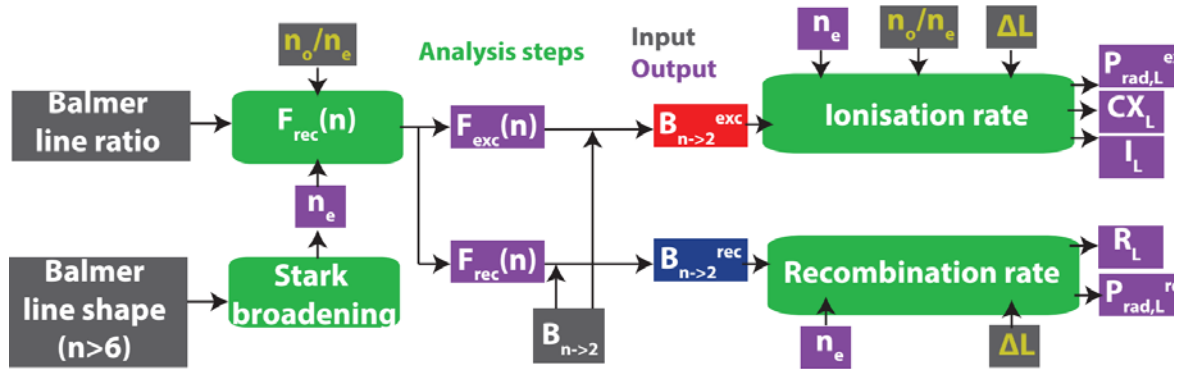


Figure 2: Schematic overview of recombination and ionisation rate analysis methodology. Inputs are shaded in grey, assumed inputs have yellow symbols, outputs in purple, analysis steps in green.

emission [27, 35, 44].

$F_{rec}(n)$ and $F_{exc}(n)$ are then combined with the absolute Balmer line intensity $B_{n \rightarrow 2}$ to obtain the absolute Balmer line emission due to recombination and excitation ($B_{n \rightarrow 2}^{rec}$, $B_{n \rightarrow 2}^{exc}$). These are then used [35] to obtain the recombination (R_L in rec/m²s) and ionization (I_L in ion/m²s) rates (respectively), as well as the radiative power loss due to excitation and recombination ($P_{rad,L}^{exc}$, $P_{rad,L}^{rec}$ in W/m², respectively). Those chordal-integrated parameters can then, provided one has a full coverage of the (outer) divertor, be toroidally/poloially integrated (using the technique in [23, 35]) to provide the total (outer) divertor recombination rate I_r (in rec/s); ionisation rate I_i (in ion/s); hydrogenic excitation radiated power P_{rad}^{exc} in W; hydrogenic recombinative radiated power P_{rad}^{rec} in W. The analysis also can provide a measure of the local (along a chord) ‘characteristic’ excitation/recombination

temperature (T_e^E , T_e^R , respectively). Those can be interpreted as emission-weighted temperatures along the line of sight [35]. Using the excitation temperature T_e^E and assuming that excitation and charge exchange occur at the same location of the chordal integral, an estimate of the line integrated charge exchange to ionisation ratio CX_L/I_L can be obtained. Further information on all the various output parameters can be found in [44] – table 1.

As shown in Figure 2, several input parameters (e.g. neutral fraction n_o/n_e , pathlength ΔL) are required and assumptions must be made to characterize them – see table 2 [44] for an overview. The assumed uncertainty can be larger than 100% for some of those parameters - e.g. neutral fraction which is assumed to be in the range of 0.001 – 0.05. The effect is that a Taylor-expansion based error analysis is insufficient to accurately estimate uncertainties of the inferred output parameters. We thus developed and used a Monte-Carlo based probabilistic analysis [35] to estimate output quantities and their uncertainties. This works by ascribing to every single input parameter in the analysis a probability density function (PDF) characterising their uncertainties. Using rejection sampling, random values according to those PDFs are chosen on which the analysis is performed. This, eventually, leads to a distribution of different output parameters which can be mapped to a probability distribution for the output parameters [45]. Using those output PDFs, an estimate of the output value and its uncertainty (Highest Density Interval) are obtained using techniques adopted from Bayesian analysis [46] - (Maximum Likelihood / Highest Density Interval [47]). See [35] for a full overview of this probabilistic technique and for examples of output PDFs.

The above analysis is based on a Balmer line slab model for the Balmer line brightness ($B_{n \rightarrow 2}$ in ph/m^2 s with upper quantum number n) - Equation 4; is a function of path length (ΔL), electron density (n_e), neutral density (n_o) and temperature (T_e) using the Photon Emissivity Coefficients ($PEC_{n \rightarrow 2}^{rec}$) for recombination and excitation ($PEC_{n \rightarrow 2}^{exc}$), obtained from the Open-ADAS database [48, 49].

$$B_{n \rightarrow 2} = \underbrace{\Delta L n_e^2 PEC_{n \rightarrow 2}^{rec}(n_e, T_e)}_{B_{n \rightarrow 2}^{rec}} + \underbrace{\Delta L n_e n_o PEC_{n \rightarrow 2}^{exc}(n_e, T_e)}_{B_{n \rightarrow 2}^{exc}} \quad (4)$$

Here it is assumed that: a) molecular reaction contributions to the Balmer line emission are negligible (they can however strongly contribute to D_α [36]); b) the Balmer line emission originates from a plasma slab with spatially constant parameters (OD model) with a chord intersection length of ΔL ; c) the hydrogen ion density equals the electron density (e.g. $Z_{eff} = 1$) – which introduces insignificant errors on the analysis shown below [27]. Deviations between the inferred parameters and actual parameters can occur due to the above assumptions as well as ‘line integration effects’: artefacts in the analysis output arising from the fact that the chord integrates through a plasma with spatial profiles rather than the OD slab model presented in Equation 4. This has been investigated in detail in [35] – indicating that the analysis is insensitive to the mentioned assumptions as well as line integration effects. The insensitivity is determined by using a synthetic diagnostic approach applied to SOLPS simulations [35] as well as by using more simplified a priori model with assumed n_e , T_e profiles [27]; deviations between inferred parameters and actual parameters remain smaller than the characteristic uncertainties of the inferred parameters [35].

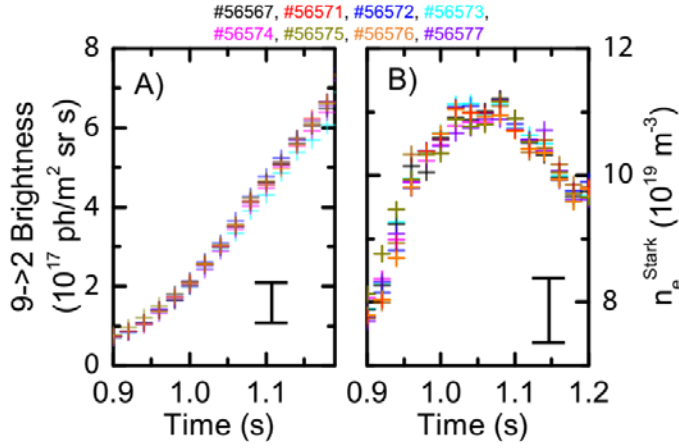


Figure 3: a) 9->2 Balmer line brightness and b) inferred Stark density from the 9->2 Balmer line obtained from the vertical system using the line of sight closest to the strike point location. Each colour indicates a different discharge. Characteristic uncertainties are shown in the Figure.

measurements for a set of 8 sequential identical discharges (of which #56567 is studied extensively in this paper) using the vertical DSS spectrometer from the line of sight corresponding to the strike point. The time dependencies of Balmer $n=9$ line intensity (Figure 3a) and the derived chordal averaged (weighted by the $n=9$ (recombinative) emission profile) density (Figure 3b) are the same within uncertainty from discharge to discharge. In addition, results from other diagnostics (bolometry and Langmuir probes – not shown) also agree within uncertainty for the repeated discharges, indicating enough reproducibility for our primary measurements of the divertor plasma characteristics. The reproducibility can be significantly worse if discharges are repeated on different days.

3. Results

Analysis of three discharges, including two core density ramps (at two different plasma currents) and a nitrogen seeding ramp, show that the ionization source is the primary process that determines the target ion current and its reduction at detachment in TCV, whereas the role of recombination as an ion sink remains secondary for the analysed TCV discharges. In any case, our results indicate that under all (high-recycling) conditions ionisation source reduction must occur before volumetric recombination can become significant. The magnetic geometries for the three cases are shown in Figure 1a and table 1 gives their key parameters. All discharges are in L-mode without additional heating and are performed in reversed field (e.g. ∇B in the unfavourable direction) to stay out of H-mode.

Analyses of just the power balance, utilizing hydrogenic and total radiation estimates, show that the power reaching the recycling region, P_{recl} , is *reduced* during a density ramp discharge due to increasing impurity radiation. This power can also be taken as the maximum power ‘available for ionisation’ [14, 18]. In contrast, the power ‘required for ionization’, P_{ion} , *increases* during the pulse until $P_{\text{ion}} \sim P_{\text{recl}}$ to within experimental uncertainties, which approximately correlates with the roll-over point for the target ion current; this suggests that the ion source is limited by the available power. The role of pressure and momentum loss will be covered in section 4.

3.1 Detachment characteristics on TCV

First, it is important to characterize the development of ion target current loss during detachment. Secondly, we describe the development of the poloidal profiles of plasma characteristics (e.g. density,

2.2 Reproducibility of repeat discharges

At sufficiently high electron densities and recombination rates, both low- and high- n Balmer lines are needed to use the above techniques (section 2.1) to infer excitation and ionisation rates as was explained in [35]. To facilitate both measurements, diagnostic repeats are required, and thus the reproducibility of repeat discharges must be verified. To demonstrate such reproducibility we show, in Figure 3, the variation of the brightness and Stark density

radiation, recombination, ...) during detachment experimentally, which are also compared with equivalent synthetic measurements [35] performed on the corresponding SOLPS plasma solutions [28]. Previous studies have provided complementary descriptions of the development of detachment in TCV [20, 27, 50-52] and are thus useful for further details.

3.1.1 Characterization of target ion loss

Density ramp experiments use feedback control of the D_2 fuelling to obtain a linear increase of the line averaged core density, \bar{n}_e , measured by a vertical FIR interferometer chord. \bar{n}_e is increased until

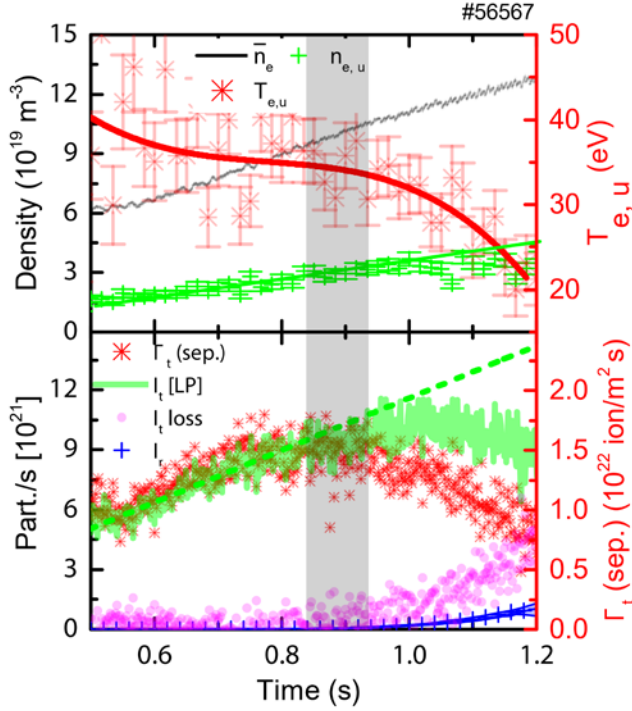


Figure 4: Overview of detachment based on a high I_p density ramp discharge (#56567). a) Line averaged, \bar{n}_e , upstream density, $n_{e,u}$ and upstream temperature, $T_{e,u}$ as function of time. b) Total ion target flux (I_t), ion target flux density at the separatrix (Γ_t), recombination rate (I_r) and I_t loss as function of time. The onset of detachment phase ($\sim 0.82-0.87$ s) is indicated as a black shaded region in this Figure and all subsequent experimental Figures as function of time.

the plasma disrupts at $t=1.25$ s, achieving maximum Greenwald fractions of ~ 0.65 . Both the total ion target flux integrated across the divertor target, I_t in ion/s, and the target ion flux density at the separatrix (Γ_t in ion/m² s) (Figure 4b), initially increase linearly with both the line-averaged and separatrix density, n_{eu} (Figure 4a). At $\sim 0.82-0.87$ s, Γ_t starts to roll-over while I_t starts to deviate from its linear trend; we use that deviation to define the onset of the process of detachment. Later, we will show that this time is in accordance with detachment onset predictions (section 4.2) and corresponds to when the ionisation profile peak lifts off the target (section 3.1.2). Note that the I_t roll-over (negative slope in I_t) can occur after the point where I_t starts to deviate from its linear trend. The separation between the deviation and rollover times (see Figure 7d-f) can vary from one discharge to another.

The linear scaling of I_t and Γ_t with the upstream/core density for attached plasmas was observed for all the density

ramp studies at TCV [51]. This contrasts the $\Gamma_t \propto n_{eu}^2$ scaling that is fit to Γ_t data in other tokamaks [6, 53]. Further analysis in section 4.2.1 will show this linear increase of I_t and Γ_t is expected when considering the reduction of upstream temperature and the increase in divertor radiation throughout the discharge. To quantify the loss of target ion current for this study we determine a linear, in upstream density and thus time, fit to the ion target current during the attached phase and extrapolate into the detached phase. The ' I_t loss' is then the difference from this to the measured ion target current, I_t (see Figure 4b).

Although spectroscopic signatures of recombination start to appear just before the ion target flux roll-over, the I_t loss is significantly larger than the total recombination sink integrated over the entire outer leg (Figure 4b), indicating recombination alone is insufficient (at least by a factor three) to fully explain the I_t roll-over. This observation is general on TCV ([27] and section 3.2) and has also been observed under higher density conditions in Alcator C-Mod [7] as well as under N_2 seeded conditions [34].

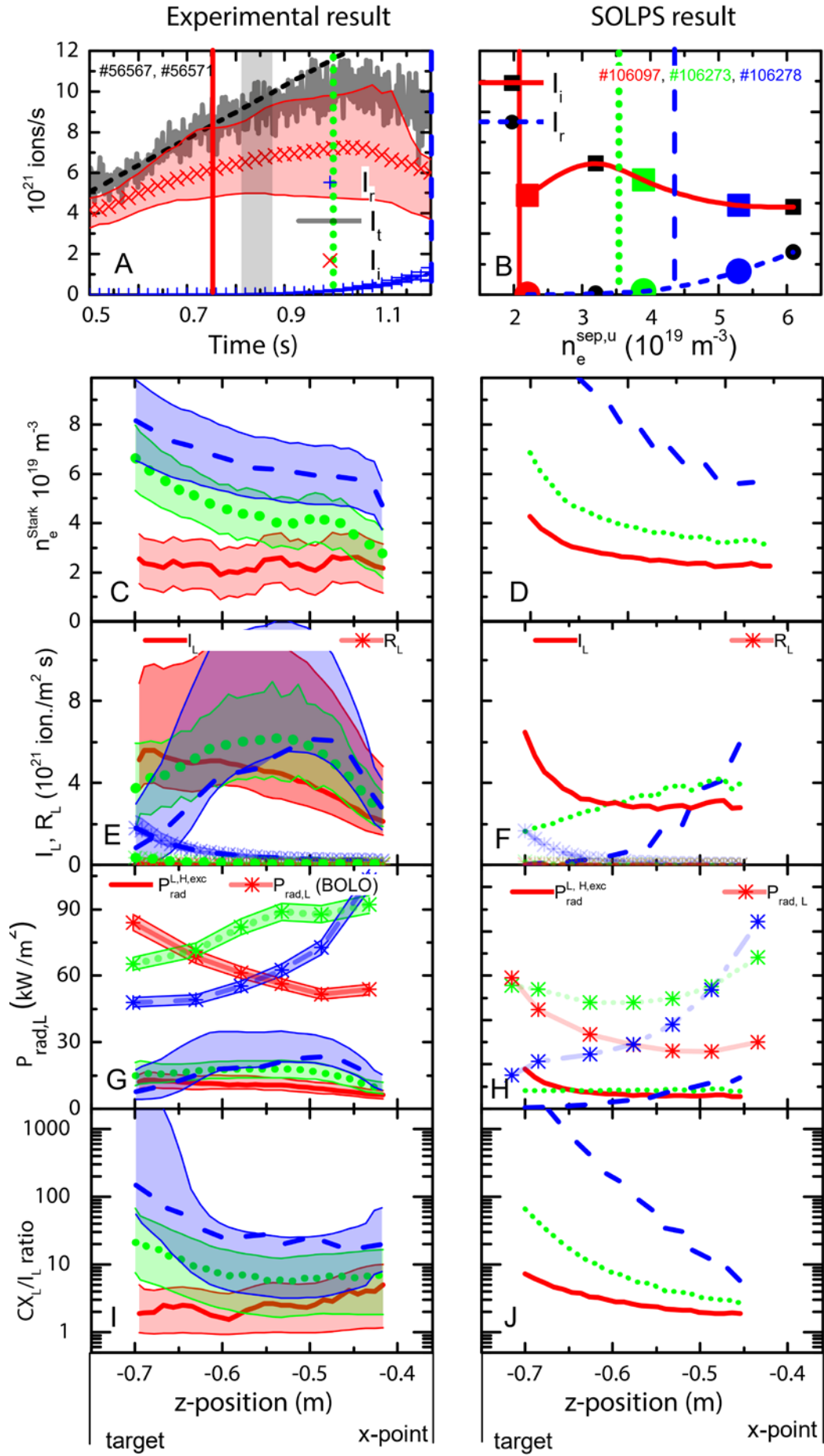
3.1.2 Experimentally observed TCV detachment dynamics and corresponding SOLPS solutions

During the periods before, during and after the target ion current roll over (~ 1 s) the experimentally-measured poloidal profiles of several plasma parameters along the outer divertor leg vary (Figure 5c,e,g,i). The profile times correspond to the vertical lines in Figure 5a. The equivalent density scan modelled using SOLPS is shown in Figure 5b. This simulation [27] does not reproduce the experimental result that the upstream density saturates upon detachment. As such, a linear trend of the upstream density has been used to match the chosen times to the appropriate n_{eu} . The three SOLPS simulations used to compare to experimental profiles are indicated by the enlarged symbols in Figure 5b, where their colours correspond to the vertical lines at which the experimental data is taken, shown in Figure 5a. The SOLPS profile results (Figure 5f, h, j) are obtained by integrating through the 2D SOLPS profiles of ionisation, recombination, etc.) along the DSS and bolometric viewing chords (Figure 5h - $P_{rad,L}$), enabling a closer comparison between experiment and simulation. The divertor-integrated results (Figure 5f) are obtained by integrating the ionisation source/recombination sink from SOLPS over the region covered by the entire horizontal DSS horizontal viewing chord fan (Figure 1a). The SOLPS ‘Stark density’ result (Figure 5d) for each viewing chord is obtained from a synthetic DSS diagnostic. Further details of how the synthetic measurements created from SOLPS output are provided in appendix A1.

Before detachment, the density along the divertor leg (Figure 5c), the radiated power (Figure 5g – $P_{rad,L}$) and recombination rate (Figure 5e – R_L) all peak near the target. Further increases in \bar{n}_e and $n_{e,u}$ generate a gradual shift in the radiated power peak towards the x-point, followed by a displacement of the peak in the ionization region (Figure 5e – I_L). The process of detachment starts to occur when the ionization peak lifts off the target, corresponding to a flattening of the measured ion target current (starts at ~ 0.83 s Figure 5a). As the ionization moves away from the target a region where charge exchange dominates over ionisation is left behind (Figure 5i), eventually extending over a region up to ~ 20 cm from the target. During the entire detached phase, both the Stark density and recombination rate continue to increase across the entire divertor leg whilst their peaks remain near the target (Figure 5c,e) where the lowest DSS measurement chord is ~ 5 cm above the target surface. At the highest core density, recombination dominates over ionisation only over a small region (<10 cm) close to the target (Figure 5e).

All of the above observations are in excellent qualitative (and in most cases even quantitative) agreement with the SOLPS simulation results.

Figure 5: Left hand side: Experimentally (spectroscopic inferences + bolometry) determined quantities along the outer divertor leg. Right hand side: Results obtained directly from SOLPS simulation utilizing synthetic diagnostic measurements. a) Total ion target flux, outer divertor integrated ion source and recombination rate (I_i , I_r), together with the linear scaling of the ion target flux as function of time and vertical lines corresponding to the times at which the profiles are shown in the Figures below. b) Analogous ion source/sink plot (outer divertor integrated) obtained from SOLPS where the ionisation source and recombination sinks are shown as function of upstream density. c, d) Stark density profiles (c – obtained from a synthetic diagnostic – see Appendix A.1). e, f) Chordal integrated recombination (R_L) /ionisation rate (I_L) profiles. g, h) Chordal integrated total radiation profiles through bolometry – $P_{rad,L}$ and radiation due to hydrogenic excitation – $P_{rad,L}^{H,exc}$. i, j) Line integrated charge exchange (CX_L) to ionisation ratio (I_L) profiles.



3.1.3 The dynamics of the electron density in the divertor during detachment

The three time points in the general plasma characteristic profiles along the divertor leg (Figure 5c, f, g, h) provide a coarse temporal resolution and therefore do not fully convey the dynamics of the electron density near the target, which we expect, based on previous work [2, 25, 54], to drop as the low pressure/density regions expand from the target towards the x-point during detachment.

Stark density measurements from the 7 horizontal DSS viewing chords closest to the target are shown in Figure 6a together with the viewing geometry (Figure 6b). This discharge is similar to the one discussed in sections 3.1.1 and 3.1.2, but with a magnetic geometry optimised for DSS strike point coverage. At approximately the time of the total ion target current roll-over (~ 0.87 s), which coincides with the time where the ion target flux deviates from its linear trend (not shown), the measured Stark density for the viewing chord nearest to the target rises above the peak density measured by Langmuir probes at the target (Figure 6a). Afterwards, when the core density is further increased, the Stark density (within ~ 5 cm from the target) peaks after which it rolls-over, which happens after the ion target current roll-over and after the target density peak (Langmuir probes, Figure 6a) starts dropping. This data is consistent with observations from the vertical DSS system indicating a reduction in line averaged ($9 \rightarrow 2$ Balmer line, thus recombination emission weighted) density throughout the divertor leg (Figure 3b). Since the density peak must have started at the target before detachment, the strong decreasing trend of the lowest viewing chord density would be consistent with the density peak *starting to move up* along the leg.

There is a concern that the Langmuir probe measurement of the target density is incorrectly low. Since the Langmuir probe density inference uses the Langmuir probe-derived temperature ($J_{sat} \propto n_e^{LP} \sqrt{T_e^{LP}}$), the density would be underestimated when T_e^{LP} is overestimated – which generally occurs

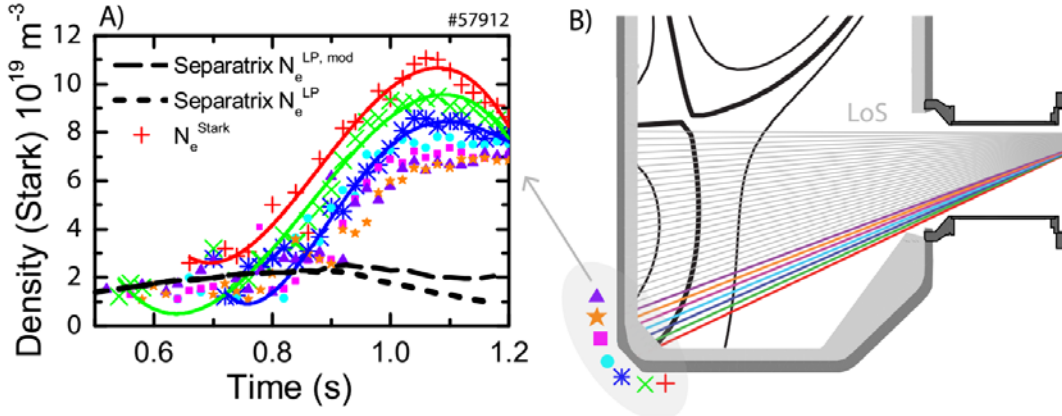


Figure 6: A) Electron density (characteristic uncertainty $\sim 10^{19} \text{ m}^{-3}$) traces density from target Langmuir probes and DSS chords near the target (#57912) for a density ramp experiment. B) Divertor geometry and line of sights corresponding to the DSS measurements.

in cold divertor conditions [38, 55, 56]. As such, following a similar approach as in [27], we calculated

a modified $n_e^{LP, mod} = n_e^{LP} \sqrt{\frac{T_e^E}{T_e^{LP}}}$ using a spectroscopically inferred T_e^E (section 4.1.1) from the excitation emission of the chord closest to the target (Figure 6a). $n_e^{LP, mod}$ remains significantly smaller than the observed Stark density upon detachment. Some combination of the width of the poloidal viewing chord (1-2 cm) and the weighting of the Stark density towards the higher densities (and thus higher emissivities) along the cone describing the target line of sight is driving this difference. This discrepancy thus suggests that the electron density strongly decreases in a narrow region (< 2 cm)

close to the target. The Stark electron densities in low temperature conditions could be overestimated (by up to $2 \cdot 10^{19} \text{ m}^{-3}$ at the end of the discharge shown) according to certain Stark models [57], due to the electron temperature dependence of the Stark width [36]. A decay of the electron density in such a narrow region during detachment is also observed in the SOLPS simulations [28], although the amount the electron density decays ($1\text{-}2 \cdot 10^{19} \text{ m}^{-3}$) appears to be smaller.

3.2 Characterization of the loss of ion source and its effect on the ion target flux
In the survey of discharge characteristics (Figure 4), the inferred ionization source magnitude and time dependence appears to determine the current reaching the target. The following discussions are based on particle balance over the entire divertor and not just a particular flux tube. The balance of sources and sinks *within* the divertor can be written:

$$I_t \approx I_i - I_r \quad (5)$$

where the target ion flux (the sink for ions at the target), I_t , is the sum over the divertor target surface while both the ionization source, I_i , and the volumetric recombination sink, I_r , are integrated over the entire outer divertor leg. Equation 5 assumes the divertor to be a closed, self-contained, system where the total divertor ion target current is dominated by divertor ion sources, ignoring sources of ions outside the divertor (core or SOL ionization) which flow from upstream towards the target; an approach used previously [7, 10, 11] and we will discuss it further in section 3.3. In this paper we define the divertor to be ‘high recycling’ when this condition (Equation 5) is valid.

3.2.1 Characterization of ion sinks and sources in density ramp discharges

We show examples of the equivalence of the divertor ionization source and target ion current in the first two columns of Figure 7 for density ramp discharges at two different plasma currents. The ionisation source (Figure 7b & e), I_i , tracks the increasing target flux, I_t , (within uncertainties) during the attached phase for both density ramp cases while recombination, I_r , is either negligible (Figure 13d) or small (Figure 7e). We conclude that the majority of ion target flux derives from ionisation within the divertor, in agreement with the self-contained divertor approximation (Equation 5), which shows that TCV is operating under ‘high recycling’ conditions. These measurements also indicate that any additional source of ion flux from the SOL into the divertor should be either relatively small or balanced by the ion flux flowing from the outer divertor towards the inner target.

High recycling divertor operation has been illustrated as a narrow ionisation region in front of the target [4]. This contrasts with our TCV observation (Figure 5). The difference in ionisation layer size is likely due to the large mean free path of ionisation on TCV (5-10 cm). This indicates that having a narrow ionisation region may not be necessarily a requirement for cases where Equation 5 applies.

The various ion losses for the density ramp cases can be compared quantitatively by assuming that both the ion target flux and I_i should increase linearly with time for the density ramp discharges (red dashed lines Figure 7b, e). The losses are then calculated by subtracting the measured I_t and I_i from these respective linear scalings. The measured target ion current loss and the ionization source loss track well within uncertainties for both density ramp cases (Figures 7c, f). The recombination ion sink is only significant at the end of the high plasma current discharge; it only starts to develop to significant levels after the ion target flux roll-over and long after the deviation of the measured I_t from its linear (attached) scaling and it remains more than a factor 4 lower than the loss of target ion current or loss of ionization source.

There is a clear difference in the role volumetric recombination plays between the low and high current cases. This is an interesting observation, as it suggests that (for the same core Greenwald

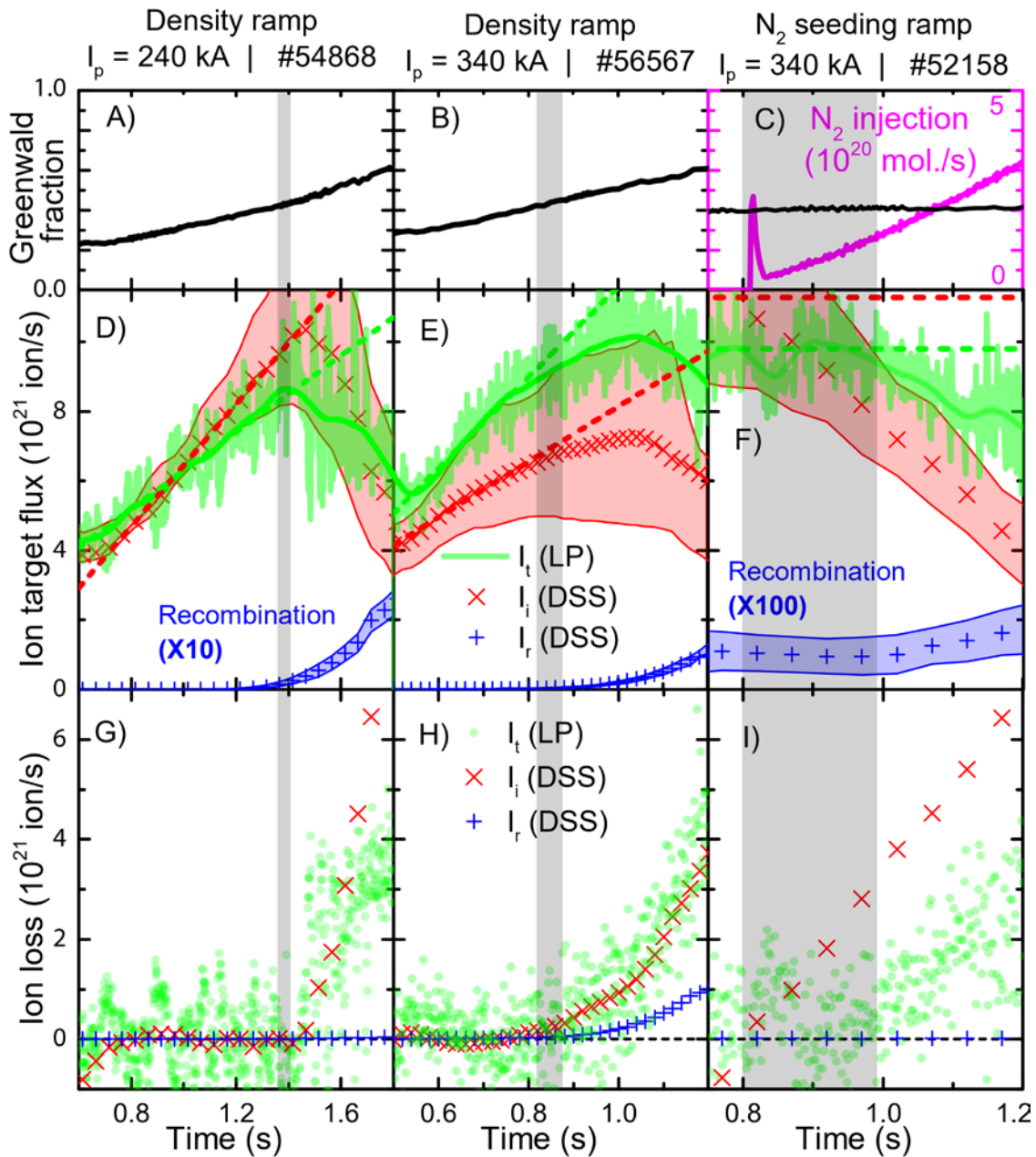


Figure 7 – First two columns correspond to core density ramps at two different plasma currents: Core Greenwald fraction (a,b); divertor ion sources/sinks and ion target flux (d, e) as well as the loss of ion target current, recombination sink and loss of ionization (g, h). The last column corresponds to a N_2 seeding ramp at constant core density (c): divertor ion source/sink and ion target flux (f) as well as the loss of ion target current, recombination sink and loss of ionization (i).

fraction) the plasma current is a ‘control knob’ for the influence of recombination on the ion target flux. The recombination rate in the high current case is 5-10 times higher at the same core Greenwald fraction as in the lower current case. One explanation for the higher recombination rates is that the $\sim 1.5 \times$ higher n_{eu} leads to higher divertor densities. These are observed (Stark density) to be $\sim 3 \times$ higher for the high current case, which agrees with the expected strong dependence of the divertor density on n_{eu} (cubic, based on the two point model [4]). Assuming identical divertor temperatures between

the two cases, this would result in $\times \sim 10$ times higher recombination rates (estimated from ADAS tables [48, 49]).

3.2.2 Characterization of ion sinks and sources in N₂-seeded discharges

N₂ seeded discharges develop significantly differently than the core density ramp discharges discussed previously. The line averaged density for this pulse (Figure 7g) is held constant over the N₂-seeding ramp at a Greenwald fraction of ~ 0.4 . This is just below the core density at which the ion target flux roll-over occurred in the equivalent high current, density ramp discharge (pulse #56567; Figure 7 d-f). The ion target loss is quantified as previously using the pre-N₂ seeding scaling as a reference. This likely underestimates the actual value of the ion target loss as in attached conditions the ion target flux is expected to increase if impurity radiation in the divertor is altered while other divertor parameters are kept constant (Equation A.8). The magnitude of the ion source loss, including the range of uncertainty, was larger than that needed to explain the magnitude of the ion target flux.

We can only speculate as to why the particle balance between sinks and sources is not as consistent for the case of N₂-seeding. One possible explanation is that a significant fraction of the target ion current was carried by nitrogen ions, thus contributing a significant fraction of the ion target current. To explain the mismatch between the ion target flux and the ionisation source prediction, a nitrogen concentration of 10 - 25% would suffice assuming an average nitrogen ion charge of 2. A crude analysis, using Open-ADAS photon emission coefficients together with the NII (399.6 nm) line brightness measured by the DSS and $(T_e^E, n_e, \Delta L)$ obtained from the Balmer line analysis, indicates the ratio between the N⁺ density and n_e is larger than 4%. The total nitrogen concentration is likely significantly higher than the N⁺ concentration: to illustrate, for a transport-less plasma – which is not valid here – one would expect a fractional abundance of N⁺ smaller than 0.1 for the values for T_e^E obtained). This crude analysis is consistent with the explanation of a significant portion of the ion target current being due to nitrogen ions but does not constitute a proof. A proof would require a more quantitative and complicated analysis as in [58].

3.3 Power balance in the divertor and relationship to ionization

We have now described all the elements in divertor particle balance using our estimations of the ionization source in combination with the ion sinks at the target and in the plasma. The divertor ion source is approximately equal to the target ion current; this suggests that the divertor ion source, I_i , is the main determinant of the ion target flux from a particle balance point of view (remembering that p_t must also drop). It has been suggested previously, both experimentally [7] and theoretically [10, 11, 30] that the ion source can be limited by the amount of power available for ionization in the divertor. To address directly whether power limitation of the ion source leads to the ion source behaviour we now develop a power balance analysis and apply it to the outer divertor for one of the discharges shown in Figure 7, #56567.

The power entering the divertor, P_{div} , is lost partially to radiation, P_{rad} , after which the remaining power ends up at the target (P_{target}), both in the form of potential energy, $P_{target}^{pot} = I_t \epsilon$ and kinetic energy, $P_{target}^{kin} = I_t \gamma T_t$, where $\gamma \sim 7$ is the sheath transmission factor. This is shown in Equation 6, where $\epsilon = 13.6$ eV is the potential energy and again the molecular dissociation potential of 2.2 eV [1] is neglected.

$$P_{div} - P_{rad} = P_{target} = I_t(\gamma T_t + \epsilon) \quad (6)$$

The radiated power highlighted in Equation 6 can be split into different portions: hydrogenic radiation and impurity radiation. Hydrogenic radiation has both an excitation ($P_{rad}^{H,exc}$) and a recombination ($P_{rad}^{H,rec}$) contribution. The split of radiated power is

$$P_{div} - P_{rad}^{H,exc} - P_{rad}^{H,rec} - P_{rad}^{imp} = I_t(\gamma T_t + \epsilon) \quad (7)$$

To obtain further insight into the power loss processes, we can re-arrange Equation 7 by bringing the potential energy of the ions reaching the target to the other side of the Equation and utilising the closed box approximation (Equation 5):

$$(P_{div} - P_{rad}^{imp}) - (P_{rad}^{H,exc} + \epsilon I_i) - (P_{rad}^{H,rec} - \epsilon I_r) = I_t \gamma T_t \quad (8)$$

We have already grouped several terms for explaining the processes in divertor power balance, which are schematically shown in Figure 8. Note that the different regions in Figure 8 spatially overlap as shown in section 3.1.2 (Figure 5). This analysis, however, does not rely on such a separation and the regions shown in Figure 8 are only intended to serve as a visualisation aid.

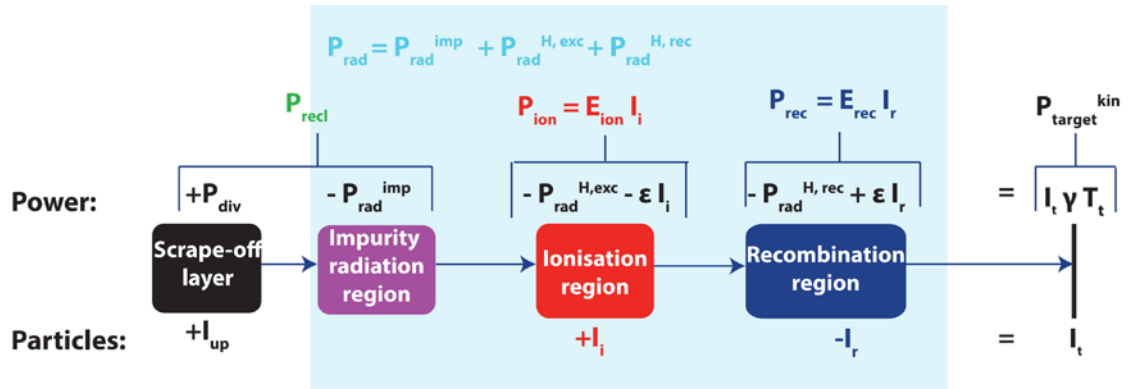


Figure 8: Schematic overview of power and particle balance in the outer divertor. The blue shaded region represents the divertor. The top line describes power balance in terms of power entering the divertor (P_{div}), impurity radiation (P_{rad}^{imp}), power reaching the recycling/ionisation region (P_{recl}), ionisation power cost (P_{ion}) and recombination power cost (P_{rec}), eventually resulting in kinetic power reaching the target (P_{target}^{kin}). The bottom line in the Figure describes particles (ion) balance in terms of an ion flow from upstream (I_{up}), ions generated in the ionisation region (I_i) and ions being removed in the recombination region (I_r), eventually leading to I_t ions reaching the target.

The power flow into the divertor, P_{div} , is first reduced through divertor impurity radiation by an amount P_{rad}^{imp} . We define P_{recl} as the power which enters the recycling region (Equation 9).

$$P_{recl} = P_{div} - P_{rad}^{imp} \quad (9)$$

While we include the effects of ionization in the power balance of the recycling region we ignore, for simplicity, energy losses due to charge exchange (CX). While the CX energy losses have been estimated per ionisation event ($\sim 3-5$ eV [10]), higher estimates for TCV parameters (5-15 eV [59]) are obtained by [14, 59]. In either case, as a sink or source of energy, the CX power loss is difficult to quantify for a simple model and we do not include it in the following. However, preliminary results from SOLPS simulations [28] indicate that CX related power losses are secondary to impurity and hydrogenic radiation.

Power is lost in the ionisation region due to excitation collisions preceding ionisation, leading to radiation losses ($P_{rad}^{H,exc}$) as well as to the potential energy conversion ϵ required for ionisation. The total ionization power loss is then provided by Equation 10. Dividing the total ionisation power loss by the total ionisation source leads to an effective ionisation energy loss, E_{ion} (Equation 11), which is an important parameter in modelling the ion target current dynamics as will be discussed in section 4.1 and 4.2. Furthermore, E_{ion} will rise during detachment as the ionisation region grows colder and more excitation collisions occur before ionisation. This is observed experimentally (section 4.1.3) to have a

significant influence on the ion current reduction during detachment (section 4.1.3) in agreement with SD1D predictions [60].

$$P_{ion} = P_{rad}^{H,exc} + \epsilon I_i \quad (10)$$

$$E_{ion} = \frac{P_{ion}}{I_i} = \frac{P_{rad}^{H,exc}}{I_i} + \epsilon \quad (11)$$

There are both energy gains and losses in the recombination process. Recombining ions can release their potential energy ($\epsilon = 13.6$ eV) back to the plasma. But, in addition, recombination leads to radiation losses, $P_{rad}^{H,rec}$, which takes all forms of recombination (radiative and three-body) into account. The total power ‘cost’ of the recombination region (P_{rec}) is thus given by Equation 12, which is similar to how the power loss/gain due to recombination in [61] was determined.

$$P_{rec} = P_{rad}^{H,rec} - \epsilon I_r \quad (12)$$

Note that if $\epsilon I_r > P_{rad}^{H,rec}$, P_{rec} will be negative and recombination will lead to a net plasma heating. Generally, recombinative plasma heating will occur when a significant portion of recombination is three-body recombination [4], which is more likely at higher electron densities and lower electron temperatures. In any case, the value of P_{rec} on TCV is small, whether slightly positive or negative (see section 4.1.3).

We now rewrite Equation 8 using the definitions of equations 9,10,12 to better visualise power balance in the recycling region and what reaches the target:

$$P_{recl} - P_{ion} - P_{rec} = P_{target}^{kin} \quad (13)$$

As P_{recl} is lowered through impurity radiation (while keeping P_{div} constant and P_{ion} rising), a point can be reached where P_{recl} limits the power needed for ionization, P_{ion} . The ionization source, I_i , would then be reduced, sometimes called a form of ‘power starvation’. A reduction of the ion source leads to less ions entering the recombination region (where more losses can occur) and thus a reduced target current, I_t . As part of this ‘power limitation’ process P_{target}^{kin} also drops and the temperature near the target drops (see Figure 8 and Equation 8), making that region conducive first to ion-neutral collisions which are related to momentum loss processes, and then, as the target temperature continues to drop, recombination.

One could imagine that the target ion current controls the upstream ion source as neutrals created at the target are needed for ionization upstream [10, 11, 14]. However, if P_{recl} is not large enough to ionize all those neutrals then they would accumulate. This appears to be the case as the target ion current is strongly reduced in detachment. The TCV divertor neutral pressure, measured by baratron gauges [51], stays high and even increases while the ion source is decreasing similar to that observed in C-Mod [62, 63]. SOLPS simulations [28] indicate that the neutral density averaged over the DSS chords (weighted by the excitation emission profile), as well as neutral pressures obtained in the simulation, increase during detachment while the neutral fraction (n_0/n_e) remains roughly constant.

To utilize the divertor power balance structure described above we also need to explain how the various parameters are obtained experimentally. First, we start with determining the power flowing into the Scrape-Off Layer (SOL) from the core plasma, P_{SOL} . Since the discharges included in this study are Ohmically heated (P_{Ohm}), P_{SOL} is obtained by subtracting the core radiated power (P_{rad}^{core}), measured by foil-bolometer arrays (see section 2 and [36]), from P_{Ohm} . The power flowing to the outer divertor is $P_{div} = \alpha P_{SOL}$, where α denotes the fraction of P_{SOL} flowing to the outer divertor. We follow a previous study [27] which found $\alpha \sim 0.5$ for the plasma conditions (flux expansion; plasma current) of #56567.

$$P_{div} = \alpha(P_{Ohm} - P_{rad}^{core}) \quad (14)$$

To obtain P_{recl} , first we need to estimate P_{rad}^{imp} , which requires separating out the impurity radiation from the hydrogenic radiation. Using Equation 7, this can be done by obtaining the divertor radiation, P_{rad} , from bolometry while estimating both the hydrogenic radiation ($P_{rad}^{H,exc}$, $P_{rad}^{H,rec}$) and P_{ion} , P_{rec} through spectroscopic means [35, 36].

$$P_{rad}^{imp} = P_{rad} - P_{rad}^{H,exc} - P_{rad}^{H,rec} \quad (15)$$

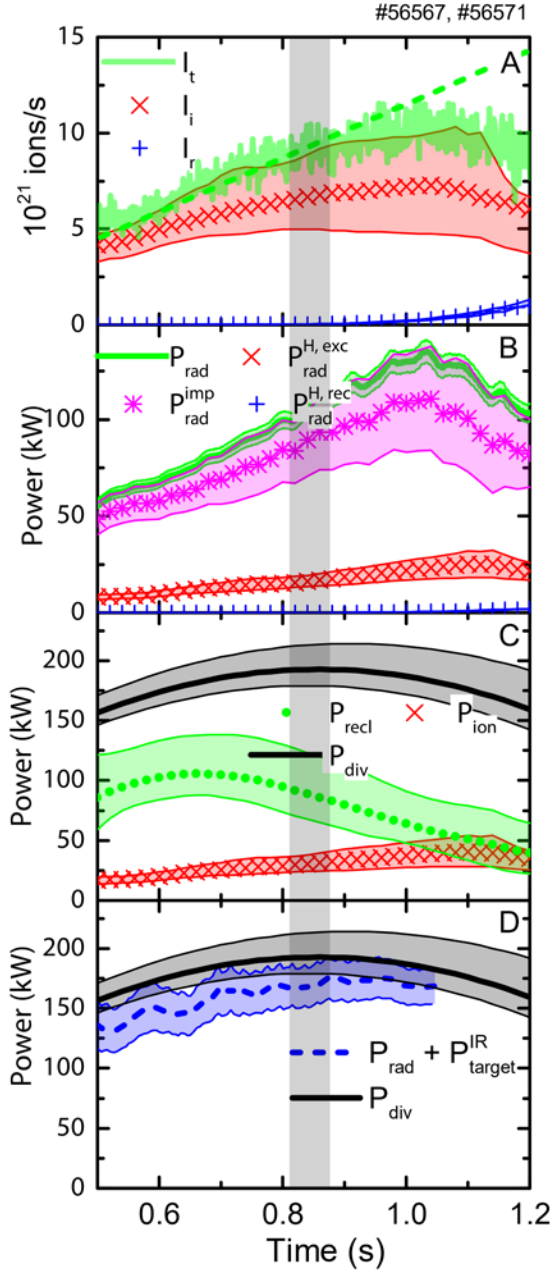


Figure 9: Power balance investigation for the outer divertor for pulse #56567 a) ion target flux, ionisation rate and recombination rate; b) break-down of total radiation and its contributors; c) comparison between power entering outer divertor leg, P_{div} , the power entering the recycling region, P_{recl} and the power needed for ionisation, P_{ion} ; d) comparison between P_{div} and the outer divertor leg radiative losses plus the measured power deposited on the target by the IR for consistency.

Figure 9 displays the result of our derivation of the various power channels for #56567; similar qualitative trends are found for the other two discharges presented in section 4.2. We include again the measurements of the target ion flux and the ionisation source (Figure 9a) along with the various divertor-integrated, power losses (Figure 9b). Impurity radiation is dominant (x 4) over $P_{rad}^{H,exc}$ with recombination radiative losses essentially ignorable.

During the ramped increase of the core and edge density P_{recl} (Figure 9c) steadily drops while the power into the outer divertor, P_{div} , remains roughly constant. This suggests that, even in non-seeded density ramp discharges, impurity radiation due to intrinsic impurities (carbon in the case of TCV) plays a key role in reducing the power reaching the recycling region in TCV, hence enabling detachment. Near the time when the ion target flux slope in time becomes negative (roll-over, $\sim 1.05s$), P_{recl} has dropped to roughly the amount of power expended for ionization, P_{ion} . This quantitative information suggests that the ion source is being limited by the power available, P_{recl} . When P_{recl} has dropped to roughly P_{ion} , $P_{target}^{kin} \ll P_{recl}$ – implying that low target temperatures are achieved as is expected from detachment and is observed (section 4.1.1). We note that P_{recl} is $\sim 2 \times P_{ion}$ when the target ion current deviates from the linear trend (~ 0.83 – $0.87s$). This makes sense as some power, beyond ionization, is required to maintain a target temperature.

Figure 9d includes a check of the overall divertor power balance. The sum of the total radiated power and the power reaching the target, $P_{rad} + P_{target}^{IR}$ (the latter term from IR measurements), is compared with the power flowing to the outer

divertor region, P_{div} , and the two match within uncertainties, giving confidence in the P_{div} determination. Note that $P_{rad} + P_{target}^{IR}$ is no longer shown after 1.05 s due to failures in the IR background subtraction algorithm.

4. Discussion

The results shown in section 3 of this paper show a strong particle balance correlation, in magnitude and time dependence, between the ionization source and the target ion current. This implies the ion current roll-over occurs due to an ion source reduction as opposed to an ion sink. In section 3.3 we also calculate that the power required to supply the measured ionisation source is approximately equal to the power flowing into the recycling region (P_{recl}); power limitation of the ionization source is occurring. P_{recl} is reduced through intrinsic impurity radiation in the divertor while the power entering the divertor remains roughly constant;

In the following discussion we utilize reduced analytic models to predict the detachment threshold and the accompanying target ion current (ion source) behaviour. These predictions are compared with observations and are used to investigate the relation between the target ion current and upstream parameters. Such reduced analytical models take the minimum number of necessary physical processes into account to model various detachment characteristics. In addition, the existence of other ion sources/sinks, apart from the ones treated in section 3, is also considered.

4.1 Investigating the ion target flux trends in the framework of power and particle balance

We now investigate the influence of ‘power limitation’ on the ion source more quantitatively by predicting the target ion source through its dependence on power and target temperature using power and particle balance [7, 11, 14] through the processes highlighted in Figure 8 & 9.

The target ion current, I_t , is calculated using Equation 16, where P_{recl} and T_t are the independent, measured, variables. Equation 16 is derived by combining the different power sinks presented in section 3.3 (Equations. 8, 11) with the closed box approximation (Equation 8). Though recombination is accounted for in particle balance, it is assumed that it is neither an energy sink nor an energy source (e.g. $P_{rec} \sim 0$ in Equation 13), which agrees with spectroscopic estimates (section 4.1.3). The predicted I_t , in this form, applies to the entire outer divertor, although this model is also applicable along a single flux tube (neglecting cross-field transport of particles and heat). Therefore T_t , the target temperature, in Eqs. 19, 20 is an effective averaged (weighted by the heat flux) target temperature [7], which is not necessarily representative of the peak temperature at the target.

$$I_t = \frac{P_{recl} - E_{ion} I_r}{E_{ion} + \gamma T_t} = \left(\frac{P_{recl}}{E_{ion}} - I_r \right) \times f_{ion}(T_t^*) \quad (16)$$

$$f_{ion}(T_t^*) = \frac{1}{1 + T_t^*} \quad (17)$$

$\frac{P_{recl}}{E_{ion}}$ represents the maximum ion source which could be achieved if all power entering the recycling region is spent on ionisation. In the absence of recombination¹, $f_{ion}(T_t^*)$ (Equation 17) represents the

¹ Equation 16 can be re-written $I_t = \beta \times \frac{P_{recl}}{E_{ion}} \times \frac{1}{1 + T_t^*}$ in which $\beta = \frac{I_t}{I_l}$ represents the fraction of ionised particles reaching the target and $\frac{1}{1 + T_t^*}$ represents the fraction of P_{recl} spent on ionisation even if recombination is present [35], in which $T_t^{**} = \beta \frac{\gamma T_t}{E_{ion}}$ represents the ratio between the kinetic power reaching the target and the power required for ionisation. For the case discussed, $\beta > 0.85$ and hence can be neglected.

fraction of P_{recl} spent on ionisation, in which $T_t^* = \frac{\gamma T_t}{E_{ion}}$ represents the ratio between kinetic power leaving the ionisation region (reaching the target) and power used for ionisation ($\frac{\Gamma_t \gamma T_t}{\Gamma_t E_{ion}}$).

It should be clearly noted that since Equation 16 requires T_t as an *input* (from a measurement): it does not take explicitly into account that changing the power entering the recycling region also influences the target temperature.

4.1.1 Target temperature estimates

The ion target flux predictions obtained using Equation 16, require an estimate of the target temperature, or more specifically T_t^* . However, obtaining the target temperature during detached conditions is challenging as T_e measured by Langmuir probes (LP) is concluded to be often overestimated in detached low T_e conditions [38, 55, 56].

An estimate of T_t can be obtained spectroscopically from the line of sight closest to the target, which yields two different target temperatures [35]: one target temperature that is characteristic of the recombinative region (T_t^R) along the chordal integral and one target temperature that is characteristic of the excitation region (T_t^E) along the chordal integral. Those are both likely an upper limit with respect to the actual target temperatures as the chord views the separatrix region at ~ 5 cm above the target. As a consistency check, these spectroscopically-derived target temperatures are compared with a target temperature derived from power balance (T_t^{PB} – Equation 18), which is obtained from Equation 7. Since T_t^{PB} is obtained from the kinetic power reaching the target, T_t^{PB} can be regarded as a heat flux averaged target temperature.

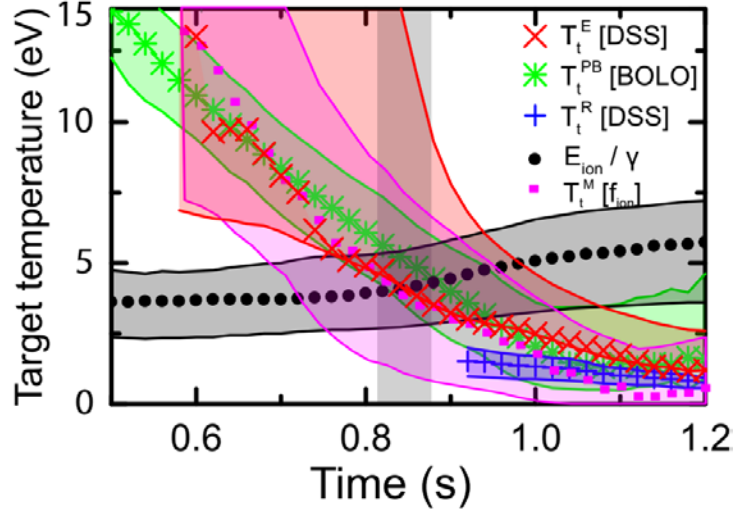


Figure 10: Target temperature estimates from spectroscopy (excitation – T_t^E ; recombination – T_t^R); power balance – T_t^{PB} and power/particle balance modelling based on the measured $f_{ion} = P_{ion}/P_{recl}$ as function of time.; T_t^M derived from f_{ion} . Discharge #56567.

$$T_t^{PB} = \frac{P_{div} - P_{rad}}{\gamma I_t} - \frac{\epsilon}{\gamma} \quad (18)$$

All three target temperature estimates show a decreasing trend as function of time, reaching target temperatures of 1-2 eV at the end of the discharge (Figure 10). T_t^E and T_t^{PB} agree within uncertainty, whereas T_t^R (shown from 0.9 s onwards, since recombinative signatures are large enough to observe at this time) starts lower and decreases less strongly as function of time. T_t^R is likely lower as recombination-dominated emission increases strongly at low temperatures and is thus dominated by contributions from lower-temperature parts of the plasma along the line of sight. We utilize T_t^E in the following prediction of the target ion flux roll-over (Equation 16). This is appropriate as the excitation emission weighted temperature, T_t , is likely similar to the heat flux averaged temperature, as most excitation near the target occurs at the highest heat fluxes.

4.1.2 Comparing the measured and predicted ion target flux

Power and particle balances, as included in Equation 16, provide a quantitative prediction of the target ion current behaviour through the attached and detached periods for pulse #56567, discussed earlier in section 3.2. This requires four input parameters: First, P_{recl} is derived from subtracting impurity

radiation losses from the power entering the outer divertor (Equation 13, section 3.3) – using P_{SOL} , bolometry and hydrogenic radiation (obtained spectroscopically) estimates. The other three

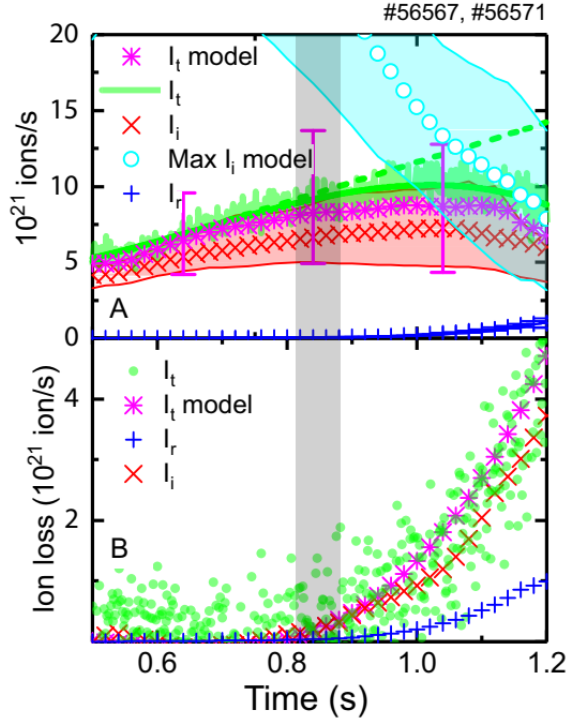


Figure 11: a) Predicted ion target flux based on power balance compared with measured ion target flux as function of time. b) Ion loss (similarly defined as in section 3.1) as function of time for the ion target flux prediction, ion source and the measured ion target flux. Pulse #56567.

parameters are E_{ion} (obtained using Equation 11, section 3.3), T_t (for which we use T_t^E), and I_r (section 3.1 - 3.2). All three latter parameters needed for equation 16 are directly determined through spectroscopic inferences [35]. The predicted ion target flux is in good agreement (in magnitude, trend and roll-over point) with experimental measurements of I_t (Figure 11a, b). This shows that the ion target flux can be described fully in terms of the maximum possible ion source, $\frac{P_{\text{recl}}}{E_{\text{ion}}}$, and the recombination sink, I_r , once T_t^* is known.

The inferred maximum possible ion source, $\frac{P_{\text{recl}}}{E_{\text{ion}}}$, is of order 2x the measured ion source (Fig. 9), I_i , at detachment (e.g. deviation of ion current trend from its linear reference which coincides with the roll-over of the separatrix ion target current for this particular discharge), which corresponds to $f_{\text{ion}} \sim 0.5$. This critical point $f_{\text{ion}} \sim 0.5$ can also be written in terms of the target temperature (Equation 17): $T_t^* \sim 1 \rightarrow T_t \sim \frac{E_{\text{ion}}}{Y}$, which occurs when the black trend crosses the red trend in Figure 10; this crossing

is in the shaded region and thus consistent with the empirical detachment threshold found in section 3.3, Figure 9 (0.83-0.87s).

The dynamics of the target ion current described by Equation 16 is a competition between two competing terms – $\left(\frac{P_{\text{recl}}}{E_{\text{ion}}} - I_r\right)$ and f_{ion} . $\left(\frac{P_{\text{recl}}}{E_{\text{ion}}} - I_r\right)$ decreases during a density ramp while f_{ion} increases, driven by both the drop in T_t and resulting increase in E_{ion} . The increase in f_{ion} is stronger in the period up to $f_{\text{ion}} \sim 0.5$, leading to a net increase in the target ion current before detachment. After detachment starts ($f_{\text{ion}} > 0.5$), the increases in f_{ion} , which are small for $T_t^* < 1$, become insufficient to fully compensate the drop of $\frac{P_{\text{recl}}}{E_{\text{ion}}}$ resulting in a flattening of I_t . The target integrated ion current roll-over starts at a higher $f_{\text{ion}} \sim 0.7$, where $T_t \sim \frac{E}{Y} \sim 2$ eV. The roll-over of the target ion current must be coincident with a reduction of target pressure faster than $T_t^{1/2}$ (equation 2). When T_t reaches this level and drops further (e.g. T_t^* approaches 0), one can approximate the target current as $I_t \sim \left(\frac{P_{\text{recl}}}{E_{\text{ion}}} - I_r\right)$. This observation is *operationally sufficient* to state that the ion source is becoming limited by the amount of power flowing into the recycling region; e.g. one can predict I_t only given $P_{\text{recl}}/E_{\text{ion}}$ and I_r . In addition, when such temperatures are achieved, volumetric recombination can become a significant ion sink.

Some might suggest that the ionization source drop is not driven by limitation of the power available, but a natural consequence of low *target* temperatures (<5 eV) where the ionisation *probability* (e.g. the number of ionisations per neutral per electron per volume) is low – so fewer ions are created.

However, such logic implicitly assumes that the neutral density and/or the power into that region is fixed. Another issue with that logic is that ionisation is a *volumetric* phenomenon and thus cannot be ascribed by only target parameters as the ionisation region expands from the target and can move all the way to the x-point.

It is true that as T_t drops, E_{ion} rises due to the additional excitations needed for each ionization; we point to this as a contributing factor in the loss in divertor ionization in section 4.1.4. However, using power/particle balance, we can make the statement that a low ($T_t < E_{ion}/\gamma$) is a *consequence* of power limitation of the ionisation source, as $P_{recl}/P_{ion} < 2$. Thus the direct cause of target ion current loss before recombination plays a significant role is power loss. This must occur coincidentally with target pressure loss (eq. 2), which is attributed (at least in part) to the formation of volumetric momentum losses – likely due to $T_t < 5$ eV.

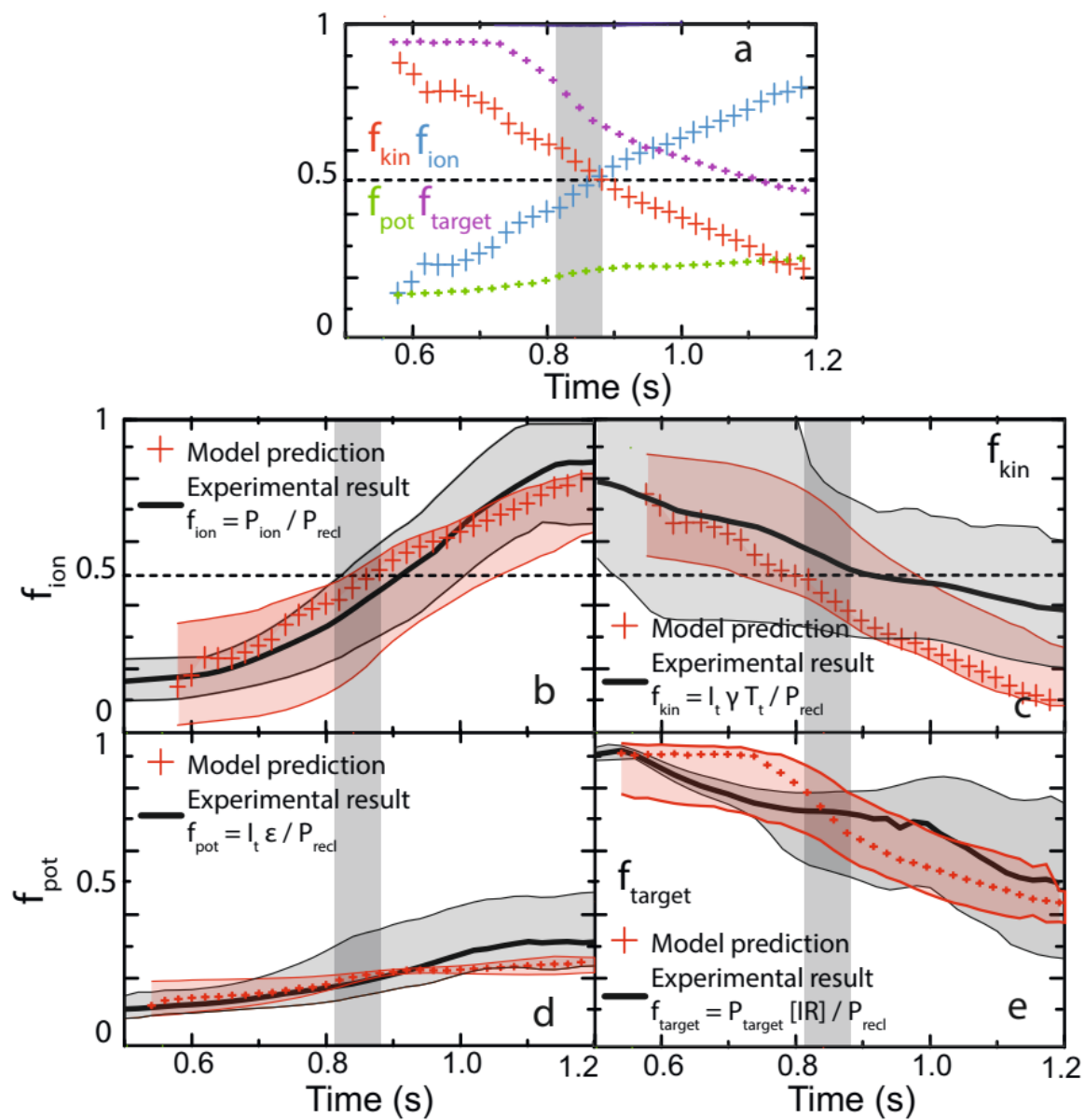


Figure 12: a) Break-down of the modelled fractions of P_{recl} spent on ionisation; reaching the target; reaching the target in the form of potential energy and reaching the target in the form of kinetic energy (based on T_t^* ; Eqs. 19, 21, 22). b-e) Comparison between the directly measured fractions with uncertainties and the modelled fractions (based on T_t^* ; Eqs. 19, 21, 22) with uncertainties.

4.1.3 Comparing the measured and predicted power fractions of ionisation

The trends in f_{ion} provide additional physical insight into the power dynamics of the recycling region and provides further means of comparing the power/particle balance model against experimental measurements. That is important as the functional form of f_{ion} (equation 17), with the sheath target condition, leads to an analytic detachment onset [10, 11, 14] prediction at $f_{ion} = 0.5$, as we will derive in section 4.2 and A.1. First, as shown in Equation 17, f_{ion} can be predicted based on T_t^* . f_{ion} can also be inferred *directly* from the experimental spectroscopic observations and power balance as $f_{ion} = P_{ion} / P_{recl}$. The experimental inference (solid lines) agrees with the predicted f_{ion} (symbols) within uncertainty (Figure 12b). Secondly, given a *measured* f_{ion} and E_{ion} , one can model T_t (labelled T_t^m) and compare it to the various experimental T_t estimates. This comparison is shown in figure 11; indicating quantitative agreement within the error bars.

Similar fractions to f_{ion} can be derived, which model the fraction of P_{recl} reaching the target in the form of kinetic/potential energy. These can be similarly compared to directly measured fractions to further validate the power/particle balance model, see Figure 12c-e. All of those directly measured fractions, analysed using a Monte Carlo probabilistic approach with uncertainties listed in [35], agree with the modelled power fractions as shown below indicating that a simple model based on T_t and E_{ion} can indeed predict the various power fractions.

Since f_{ion} is the fraction of P_{recl} spent on ionisation, we can also calculate the fraction of P_{recl} left after passing the ionisation region in the form of kinetic energy (Equation 19) – f_{kin} which is compared with a ‘directly measured’ f_{kin} , which is $f_{kin} = P_{target}^{kin} / P_{recl}$ and $P_{target}^{kin} = I_t \gamma T_t$; I_t is obtained from Langmuir probes and T_t is the target excitation temperature estimated using spectroscopic analysis – Figure 12c.

$$f_{kin} = \frac{\gamma T_t}{\gamma T_t + E_{ion}} = 1 - f_{ion} = \frac{T_t^*}{T_t^* + 1} \quad (19)$$

The other fraction of P_{recl} which reaches the target is power, in the form of *potential energy*, spent on neutral \rightarrow ion conversion (ionization) in the recycling region (ϵI_i) assuming no volumetric recombination - provided by Equation 20. Again, this modelled f_{pot} is compared with the directly estimated $f_{pot} = \frac{P_{target}^{pot}}{P_{recl}} = \frac{I_t \epsilon}{P_{recl}}$ in Figure 12c where I_t measured by Langmuir probes was used.

$$f_{pot} = \frac{\epsilon / E_{ion}}{1 + T_t^*} \quad (20)$$

The fraction of P_{recl} deposited at the target is the sum of the kinetic and potential terms: $f_{target} = f_{kin} + f_{pot}$, which decreases as function of time (Figure 12e) from 90% to 40%. That modelled value is compared with the measured $f_{target} = P_{target} / P_{recl}$, where IR measurements of the total power deposited at the target are used with an assumed 50% uncertainty on the measured P_{target} . When f_{kin} approaches 0, f_{pot} becomes the lower limit for f_{target} , and thus the power reaching the target, can attain: for $T_t^* \rightarrow 0$ and $E_{ion} \sim 40$ eV, $f_{target} \approx f_{pot} \sim 0.35$. Volume recombination (or a further increase in E_{ion}) is required for a further reduction of f_{target} .

All modelled fractions are shown in figure 12a, indicating that as the core density increases, f_{ion} increases, decreasing f_{kin} and thus f_{target} , ultimately reaching its f_{pot} limit during deep detachment at around 0.4.

4.1.3 The variation of E_{ion} in detachment

In simple modelling, the amount of energy spent per ionisation, E_{ion} , is often assumed to be constant [4, 7, 10]. The excitation radiation component ($\frac{P_{rad}^{H,exc}}{I_i}$) in E_{ion} (Equation 11) is, however, strongly

temperature dependant; as T_i is reduced, more excitations occur before an ionization happens. During the density ramp, the effective temperature in the ionisation region drops, leading to a factor of two rise in $\frac{P_{rad}^{H,exc}}{I_i} = E_{ion} - \epsilon$, the radiation cost of ionization (see Equation 11 and Figure 13b), which results in a 50% increase in the divertor leg averaged E_{ion} (weighted by the local ionisation rate).

Both hydrogenic and impurity radiation can play significant roles in reducing the number of ionizations despite the magnitude of hydrogenic radiation (through E_{ion}) being much smaller than impurity radiation, which reduces P_{recl} . This is demonstrated by the fact that the maximum ion source ($\frac{P_{recl}}{E_{ion}}$)

decreases $\sim 30\%$ between $t=1.0$ and $t=1.25$ s, due to a $\sim 10\%$ decrease in P_{recl} and a $\sim 25\%$ increase in E_{ion} .

We also investigate the divertor profile of the excitation cost of ionization ($E_{ion} - \epsilon$) along different viewing chords, $\frac{P_{rad,L}^{H,exc}}{I_L}$. Since the number of excitation events required per ionization rises strongly at low temperatures (~ 2 eV), poloidal temperature gradients lead to strong variations of $\frac{P_{rad,L}^{H,exc}}{I_L}$ along the divertor leg as shown in Figure 13c. In the region close to the target $\frac{P_{rad,L}^{H,exc}}{I_L}$ increases up to 80 eV. In hotter regions of the divertor leg (chords further away from the target), where most of the ionisations take place (Figure 13b, c), the excitation radiation cost per ionization is 15-30 eV. Variations in geometry (e.g. closed vs open divertor, vertical- vs horizontal-target), which lead to variations in recycling and neutral penetration, could influence the location of the ionisation region and thus could affect the dynamics of the target ion current loss through a change of E_{ion} , amongst other changes.

Whether recombination can heat or cool the divertor plasma is determined by the

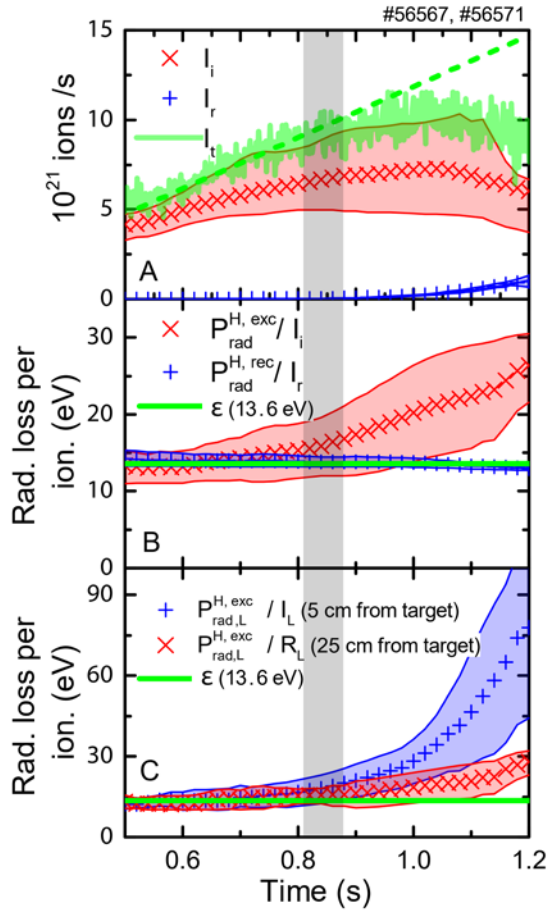


Figure 13: a) Target ion flux as function of time together with ionisation rate and recombination rate. b) Effective radiative energy cost per ionisation/recombination. c) Radiative energy cost per ionisation along a certain chord

competition between the energy loss due to recombinative radiation and the potential energy released back to the plasma upon recombination [9, 61]; as the plasma temperature and density vary the relative strength of two- and three-body recombination varies as well as the level of recombinative emission. For the TCV conditions investigated we find that the effective radiated energy loss per recombination event ($\frac{P_{rad,L}^{H,rec}}{I_R}$ Figure 13b) is roughly equal to the potential energy. That is not surprising, considering the modest TCV densities: ADAS calculations indicate an effective heating of 0 – 1 eV per

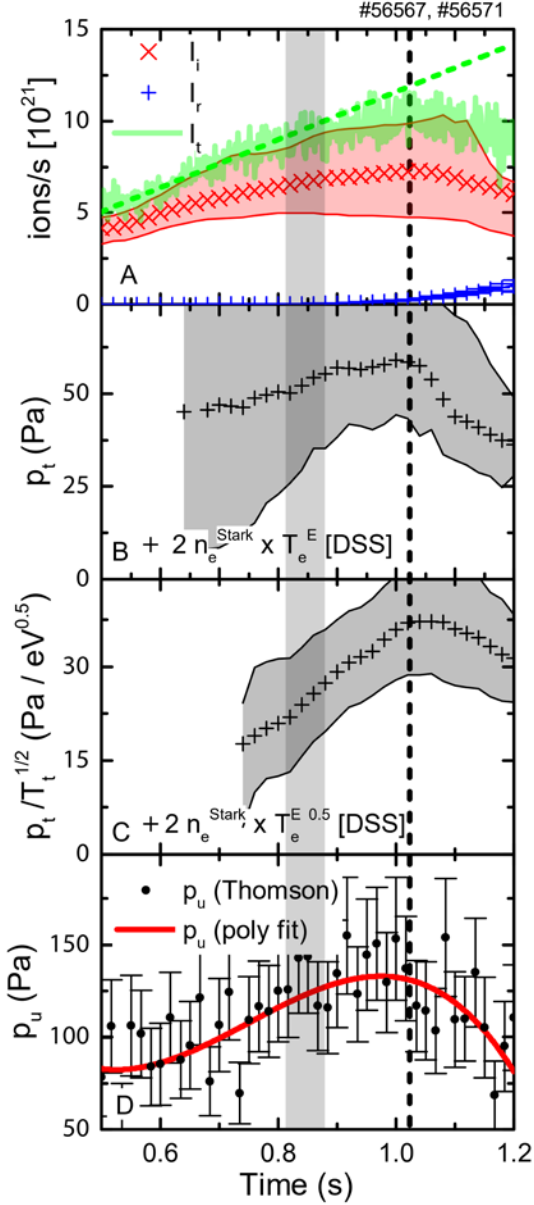


Figure 14: Comparison of target pressure and upstream pressure. a) reference total current to the target, total ionization source and recombination sink; b-c) Target separatrix pressure (p_t) and ($p_t / T_t^{1/2}$) ratio based on spectroscopic measurements (Stark broadening + excitation temperature of the chord closes to the target); d) Upstream separatrix pressure from Thomson scatterina.

upstream density saturates simultaneous with a roll-over in the upstream pressure, while the upstream temperature drops (Figure 4). As discussed in the Introduction (Equation 2), at any point during the discharge, the target ion flux scaling can be written as $\Gamma_t \propto p_t / T_t^{0.5}$, i.e. the target plasma pressure must drop faster than $T_t^{0.5}$ at the target ion flux roll-over. This is approximately observed (Figure 14 c). Following the discussion in section 4.1 (Equations. 16, 17), the target ion flux scaling (Equation 2) links the trend in the ionisation source (Equation 16) to the trend in the target pressure (Equation 2) and is thus crucial for understanding the complex interplay between momentum balance and ionisation balance. However, $p_t / T_t^{0.5}$ is expected to deviate from linear from the detachment

recombination reaction at $T_e = 1$ eV for n_e in between $10^{18} - 10^{20} \text{ m}^{-3}$, using a similar calculation as done in [61] (e.g. P_{rec} in Equation 12 divided by R_L). Hence, volumetric recombination does not lead to significant plasma heating or cooling for the TCV conditions presented.

4.2 Investigating the target ion flux trends in the framework of momentum balance

In the previous section we have investigated the target ion flux trend in the framework of power and particle balance of the entire SOL. In this section, we add momentum (pressure) balance [4, 9] to the power/particle balance analysis of section 4.1 such that the target temperature is now *predicted* instead of *set* by measurements. This enables a single flux tube comparison of the observed detachment dynamics and onset with additional predictions from simplified analytical theory; the preceding work has all been for the *entire* outer divertor. In this discussion, only the electron pressure is considered and the target pressure, p_t , is the total target pressure (e.g. twice the kinetic target pressure).

Trends in target (p_t) and upstream (p_u) electron pressure are compared in Figure 14. By assuming $p_t \sim p_u$ before detachment, p_t appears to be significantly underestimated by $\sim \times 2$. Synthetic diagnostics through SOLPS (appendix A1) indicate that this difference is due to chordal-average nature of the spectroscopically estimated target pressure. Both the upstream and target pressure are observed to roll-over at the target ion flux roll-over (Figure 14b, d). The

onset onwards, which is not the case. That discrepancy could be due to line integration effects as explained previously.

4.2.1 Modelling total target ion current behaviour with both power and momentum balance

We utilise a ‘two point’ divertor model [4], which accounts for hydrogen recycling energy losses, to model the total target ion current. We refer to this as the ‘2PMR’, discussed previously in literature [4, 10] and more extensively in [9]. See appendix A.4 for a full derivation and in A.5 we demonstrate how we apply and evaluate the 2PMR. Our first goal of the application of the 2PMR is to verify the *expected* ion target flux trend in *attached* conditions. For this, pressure constancy along a flux tube is assumed and since p_u is a set *input* to the 2PMR, the target pressure p_t is fixed as well. Under such conditions the 2PMR provides two possible solutions: one stable and one unstable. We assume in the following (section 4.2.1, 4.2.2) that the unstable solution *cannot* occur.

The 2PMR yields a relation for the target temperature (Appendix A.1 Equation A.5) as a function of E_{ion} and $\frac{p_u}{q_{recl}}$ [4, 9, 10]. We obtain the flux tube specific q_{recl} from P_{recl} (which is for the entire outer divertor) by assuming its shape is the same as the measured IR heat flux profile (see appendix A.2). The 2PMR-predicted T_t can be used to predict the target ion flux density (Γ_t in ion/s m²) on a *single* flux tube, as shown in Equation 21 (Appendix A.1 Equation A.8). It is important to note that the 2PMR Γ_t relation (Equation 21a) is *identical* to the flux surface equivalent of Equation 16 (while using the 2PMR predicted T_t - Appendix A.1), which is shown in Equation 21b for reference to the reader. The 2PMR thus connects the standard two-point divertor model with the power/particle balance model discussed in section 4.1. Here $f_{ion}\left(T_t(E_{ion}, \frac{p_u}{q_{recl}})\right)$ denotes that f_{ion} (or f_{kin}) is a function of T_t , which is a function of E_{ion} and p_u/q_{recl} (assuming pressure balance) – as discussed in appendix A.1.

$$\Gamma_t = \frac{\gamma p_u^2}{2 m_i q_{recl} f_{kin}\left(T_t(E_{ion}, \frac{p_u}{q_{recl}})\right)} \quad (21a)$$

$$\Gamma_t = \frac{q_{recl}}{E_{ion}} \times f_{ion}\left(T_t(E_{ion}, \frac{p_u}{q_{recl}})\right) \quad (21b)$$

To compare the experimental measurement of the *total* target ion current I_t (as opposed to Γ_t) to the 2PMR, we integrate Γ_t across the SOL. I_t can then be modelled using $\frac{p_u^2}{P_{recl}}$, $f_{kin}(T_t)$ and f_p (parametrising the geometric dependence of SOL profiles, which describes the influence of upstream pressure/target heat flux profiles on I_t ; see appendix A.2 Equation A.21), based on T_t predicted by the 2PMR (Equation A.10 of appendix A.1). More information is provided in appendix A.2.

$$I_t \propto \frac{f_p}{f_{kin}\left(T_t(E_{ion}, \frac{p_u}{q_{recl}})\right)} \frac{p_u^2}{P_{recl}} \quad (22)$$

The predicted target ion flux trend described by Equation 22 is similar to the measured target flux in the attached phase as shown in Figure 15a, showing a clear linear increase as function of time (and thus upstream density – section 3.1.1). Hence, simply using $I_t \propto n_{e,u}^2$, on which the “Degree of Detachment” [6], a parameter often used to investigate the magnitude of the ion current loss during detachment [20, 51], is based, is not appropriate for the TCV density ramp discharges studied, and should generally be used more carefully. In Equation 22, the main influence on I_t is $\frac{p_u^2}{P_{recl}}$ (see Figure 15b for all the terms). This basic scaling (or $\Gamma_t \propto \frac{p_u^2}{q_{recl}}$) not only arises from the 2PMR, but can also be obtained from pressure balance ($n_u T_u = 2 n_t T_t$), the sheath target Equation ($q_t \propto n_t T_t^{3/2}$) and an

equation for the target heat flux ($q_t = \Gamma_t T_t$). This results in $\Gamma_t \propto \frac{n_u^2 T_u^2}{q_t}$ (equivalent to Equation 5.13 in [4] of the basic two point model), providing an identical relation for the target ion flux as Equation 24a. Additionally, the $\Gamma_t \propto \frac{n_u^2 T_u^2}{q_t}$ scaling is also equivalent to the relation used in [6] for defining the degree of detachment originally (which is obtained by using equations 3,4,8 in [6]). Considering that scaling, even if T_u , q_{recl} , E_{ion} are held constant and only the upstream density is increased, a different scaling than $\Gamma_t \propto n_{e,u}^2$ is expected when recycling energy losses are accounted for as the power flux required for ionisation is increased at higher densities, reducing $q_t = q_{recl} f_{kin}$ in the process.

Since $I_t \propto \frac{P_u^2}{P_{recl}}$ increases linearly as n_u , $\frac{T_u^2}{P_{recl}}$ must decrease roughly as $1/n_u$. Given that P_{recl} decreases during the density ramp (Figure 9), T_u (Figure 10a) must decrease more strongly to give this scaling. As P_{div} is roughly constant throughout the discharge (Figure 9) a decrease of T_u could result from SOL broadening (which is measured by IR thermography to increase [41] by over a factor 3 until detachment is reached for the discharge shown). Alternatively, the decrease of T_u could be due to an increase in convective over conduction parallel heat transport [4].

A previous TCV study concluded that the observed linear trend of I_t with \bar{n}_e indicated that the divertor plasma was in a low-recycling operation [31]. However, given our measurements that the target ion current is dominated by the divertor ionisation source (section 4.2) and that I_t is properly predicted by the 2PMR (which assumes that all target ion current is due to divertor ionisation) strongly supports a characterization of the divertor as high-recycling.

4.2.2 Detachment thresholds and implications for momentum/pressure losses along a flux tube (separatrix)

As shown in Figure 15a, the 2PMR (where, for this case, we assume both constant pressure along the field line and a prescribed upstream pressure) can only be used to estimate I_t until 0.8 s, at which time the 2PMR, under these assumptions, reaches a ‘hard’ critical limit (appendix A.1 Eqs. A5-A6) before the ion target flux roll-over.,

It is evident from Equation 2 that the ion current roll-over, together with a fixed/decreasing target temperature, *must* be accompanied by *target pressure loss* ($p_t \propto \Gamma_t T_t^{1/2}$). The power and particle balance model discussed in section 4.1 (eqs 19,20), indicates that Γ_t is a function of T_t as there is a trade-off between using power for ionisation and the power flowing to the target expressed by f_{ion} – Equation 17. This has two implications: 1) the target pressure cannot be increased indefinitely, and a maximum exists ($p_{t,crit} = \frac{q_{recl}}{2\gamma c_s (T_t = \frac{E_{ion}}{\gamma})}$), 2) this maximum is reached at a certain threshold ($T_t <$

$\frac{E_{ion}}{\gamma}$) where further decreases in T_t lead to a smaller increase in Γ_t than predicted by the decrease in $1/T_t^{1/2}$; That critical maximum target pressure (or threshold) is reached at ~0.83-0.87 s. The changed relationship between Γ_t and $T_t^{-1/2}$ must be provided by a drop in p_t ; this corresponds to the deviation of the ion current from its linear (attached) trend. Solutions beyond this point are not allowed by the model assumptions of a fixed p_u and constant pressure along the field lines. It is thus not surprising that the 2PMR, under these assumptions, cannot model the ion current roll-over and thus only applies to *attached* conditions.

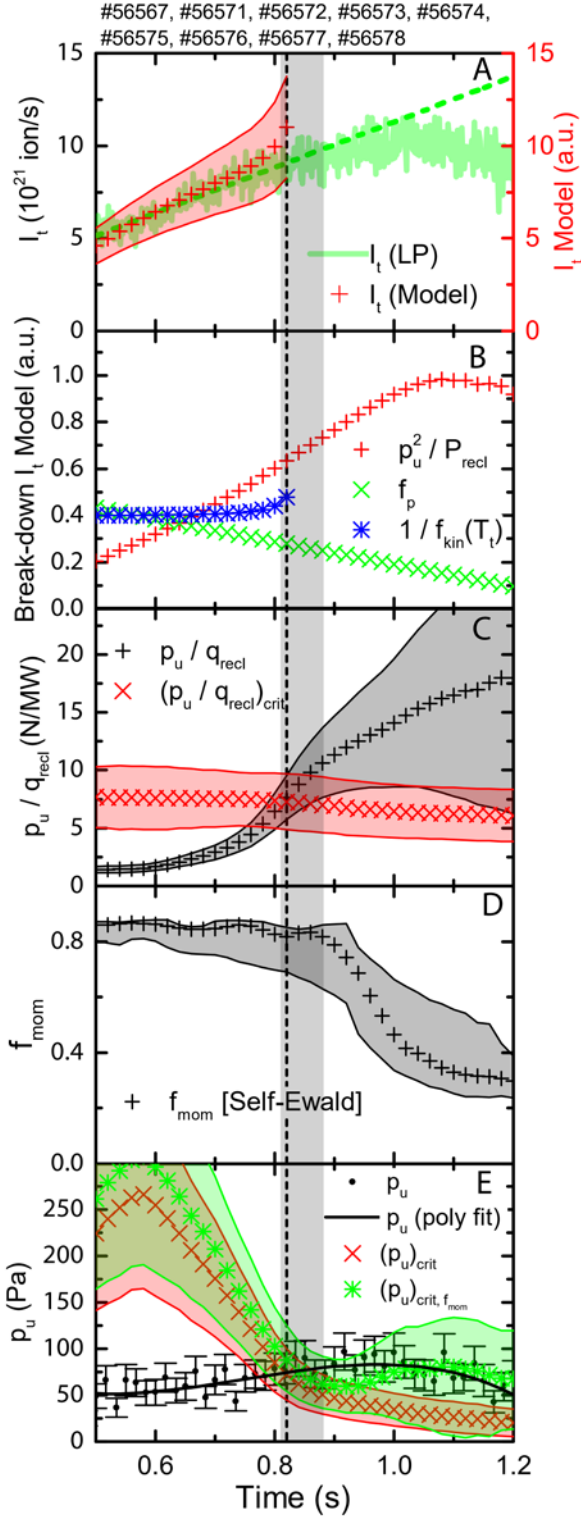


Figure 15: a) Measured and predicted target ion flux trend. b) Break-down of the contributors to the predicted ion flux. c) Measured p_u / q_{recl} compared to the critical predicted level. d) Inferred momentum losses from spectroscopic estimates. e) Measured upstream pressure compared to critical pressure level with and without momentum losses.

q_{recl} during the pulse.

The above threshold of the 2PMR model is where the target pressure is maximised and target pressure loss is necessary as Γ_t (T_t) starts to rise slower than $T_t^{1/2}$ (Equation 16, 17), has been suggested by Krasheninnikov [10, 14] to be a ‘detachment onset criterium’: for target temperatures below this limit insufficient power is transferred beyond the ionisation region to sustain a sufficiently high target temperature for the target pressure (which is collapsing) to match the upstream pressure. Stangeby, although not calling the above limits a detachment threshold, argues properly that to reach $T_t < E_{ion}/\gamma$, processes which continuously lower the target pressure as the target temperature becomes lower (e.g. the target pressure must be a specific function of the target temperature) is required [4, 9]. This can be achieved by volumetric momentum losses (as shown explicitly in [9]) and/or by assuming p_u drops as function of T_t . See appendix A.4.1 and [36] for more information.

These ‘detachment thresholds’ can be written in three different forms, given by Equation 23. We have found thresholds given in equations 23b,c experimentally (section 3.3, 4.1, Figures 9,11) to be empirical thresholds for detachment. A third (equivalent) threshold (Equation 23a) can be derived from the 2PMR (Appendix A4.1) [10] providing a critical maximum target pressure $p_{t,crit} = \frac{q_{recl}}{2\gamma c_s(T_t = \frac{E_{ion}}{\gamma})}$.

Under the assumption of pressure balance, this is commonly written [4, 10] as a critical threshold for p_u / q_{recl} , above which p_u / q_{recl} cannot rise (Equation 21a - assuming $p_t = p_u$), where c_s is the target sound speed at $T_t = \frac{E_{ion}}{\gamma}$. $(p_t / q_{recl})_{crit}$, which applies to a flux tube – not the average over the divertor, is compared to the experimentally inferred p_u / q_{recl} in Figure 15c. The increase in p_u / q_{recl} is mostly ascribable to a drop in

$$\left(\frac{p_t}{q_{recl}}\right)_{crit} = \frac{1}{\gamma c_s(T_t = \frac{E_{ion}}{\gamma})} \quad (23a)$$

$$T_{t,crit} = \frac{E_{ion}}{\gamma} \quad (23b)$$

$$f_{ion} = \frac{1}{2} \quad (23c)$$

This third critical limit (eq. 23a), evaluated at the separatrix, is also reached at ~ 0.83 - 0.87 s (Figure 15c), similar to the other detachment criteria ($f_{ion} = 0.5$ (Figure 12a), $T_t = \frac{E_{ion}}{\gamma}$ (Figure 11)) and when the integrated target ion current starts to flatten (deviate from the linearly increasing trend), the detachment process starts (Figure 10b). As discussed earlier, 0.83 - 0.87 s also corresponds to where the separatrix current *density* starts to roll-over (Figure 4b); the relative roll-over times for the total and separatrix currents is not fixed – sometimes similar but, more often, the total current roll-over time is later [51].

4.2.3 The 2PMR and pressure losses

The role of momentum loss can also be inferred from Figure 15c. The measured p_u/q_{recl} rises above the $(p_t/q_{recl})_{crit}$ threshold, which could be ascribed to volumetric momentum losses causing a separation between p_u and p_t . Defining momentum loss by $p_u f_{mom} \equiv p_t$, then the separation of p_u/q_{recl} and $(p_t/q_{recl})_{crit}$ is accounted for by $1/f_{mom}$ (Equation 24). Here we derive f_{mom} from measurements, instead of assuming a particular $f_{mom}(T_t)$ dependence (see section A.1 and [36] for more information). Introducing momentum losses in this way does not enable $T_t < \frac{E_{ion}}{\gamma}$, but does enable an ion current roll-over. More details are provided in section A.1.

$$\left(\frac{p_u}{q_{recl}}\right)_{crit} = \frac{1}{f_{mom}} \left(\frac{p_t}{q_{recl}}\right)_{crit} = \frac{1}{f_{mom} \gamma c_s(T_t = \frac{E_{ion}}{\gamma})} \quad (24)$$

From Equation 24 we find that f_{mom} would need to start to decrease from 1 at the detachment criterion to ~ 0.4 at the end of the discharge to match the measured p_u/q_{recl} (Figure 15c) to $(p_u/q_{recl})_{crit}$ in the detached phase using Equation 24. Such momentum losses in the TCV divertor during similar experiments have been determined directly from upstream and target pressure measurements [64], implying momentum losses greater than 50%.

An independent estimate of the onset and magnitude of momentum losses based solely on the dominance of charge exchange over ionisation can be made using the well-documented Self-Ewald model [3, 65] (Equation 25) which has been used in several other studies. Such an estimate assumes that the charge exchange rate equals the momentum loss rate; *e.g. each CX reaction leads to a complete loss of that ion's momentum*, which is an overestimate. Although the Self-Ewald model is an oversimplified momentum loss model, it does yield results in fair agreement with experiments and simulations [3, 14, 65]. That agreement may arise ‘accidentally’ from the temperature trend of f_{mom} predicted through the Self-Ewald model, rather than the Self-Ewald model predicting the underlying physics correctly. The Self-Ewald model does not account for other momentum sinks, such as molecular-ion collisions [65, 66] which could supply the over-estimated CX momentum losses. Although the level of momentum loss due to molecules is unknown for TCV, we do know that molecules are present and undergoing reactions in the volume of TCV (section 4.3.2). Momentum loss can also occur due to recombination. However, from a simple SOL model [67] we have evaluated the reduction of f_{mom} due to recombination for the case studied and found it negligible (smaller than 1.5% – in agreement with results from [7]). In addition, differences in transport could contribute to the observed and simulated pressure loss during detachment – or instance, cross-field transport may

‘smear-out’ pressure across the field lines, leading to a reduction in the high pressure regions near the separatrix [65].

With those caveats in mind, we integrate the spectroscopically-determined profile of charge-exchange and ionisation rates along the outer divertor leg (Figure 5e) to calculate the Self-Ewald f_{mom} as a function of time, Figure 15c. As shown in Figure 5e, charge exchange to ionisation ratios are higher near the target during detachment than elsewhere in the divertor which, in the Self-Ewald model, results in larger inferred momentum losses. Note that we use the local temperature (excitation), charge exchange and ionisation rate estimates obtained spectroscopically for each chord, instead of the target temperature (used in other studies) which we feel more accurately represents what is occurring; using the target temperature would have led to larger inferred momentum losses.

$$f_{\text{mom}} = 2 \left(\frac{\alpha}{\alpha+1} \right)^{\frac{\alpha+1}{2}} \quad (25)$$

$$\alpha = \frac{1}{1 + \frac{\int 2\pi r_i C X_L(r_i, z_i) dz}{\int 2\pi r_i I_L(r_i, z_i) dz}}$$

We utilise this approach as the relation between momentum loss and the target temperature is unknown for TCV, as opposed to a prescribed function $f_{\text{mom}}(T_t)$ as used in [4, 9, 68]. Furthermore, SOLPS simulations for TCV indicate that volumetric pressure loss can occur in the volume of the divertor [28]; not just in front of the target as observed in simulations [68] for other machines, which may invalidate making f_{mom} a function of the target temperature.

Our estimate of f_{mom} , using the Self-Ewald model, drops from ~ 0.9 to ~ 0.3 ([0.2 – 0.4] with uncertainty) is shown in Figure 15c, in agreement with the momentum losses obtained experimentally [64] and with the f_{mom} required to explain the increase of p_u/q_{recl} beyond the p_t/q_{recl} limit discussed above. This may be a coincidence – as mentioned above, the reality of CX collisions not carrying away 100% of the ion momentum may be compensated by ion-molecule collisions (not included) carrying that momentum away [66, 68].

4.2.4 The case for divertor processes reducing the upstream pressure and density

The results of the previous section show that the rise of p_u/q_{recl} beyond its critical p_t/q_{recl} limit can be attributed, at least partially, to momentum losses. However, p_u also drops during the detached phase, which will be investigated here further together with the role it plays in matching p_u/q_{recl} to its critical threshold (Equation 24). The question of what leads to the drop in upstream pressure (and density) during detachment has been discussed by several authors of analytic and modelling studies [10, 11, 13].

Recombination has been predicted to lead to saturation of the upstream density when its rate approaches the ionization rate in a flux tube through a feedback loop [69]: as n_u increases, the divertor cools further, hence augmenting the recombination sink and moving the recombination region further towards the x-point, potentially impeding a rise in n_u [69]. This is not the case for these TCV discharges as recombination remains low and can be negligible. In addition, the recombination region peak does not move far off the target (Figure 5, [27]).

Krasheninnikov [10] offers another explanation for saturation of the upstream density. During detachment, insufficient momentum losses along flux tubes can constrain, or pull down the upstream pressure. It is important to reiterate that, although an I_t roll-over requires a *target pressure* drop which increases faster than $T_t^{1/2}$ (Equation 2), analytically (from the viewpoint of the 2PMR) this can be

provided by *either* volumetric momentum loss *or* a reduction of upstream pressure (Appendix 4), or some combination.

The 2PMR predicts that there is a critical maximum target pressure $p_{t,crit} = \frac{q_{recl}}{2\gamma c_s(T_t = \frac{E_{ion}}{\gamma})}$. Given the

f_{mom} inferred from the Self-Ewald model we can predict a corresponding critical maximum *upstream pressure* ($p_{u,crit} = p_{t,crit} / f_{mom}$). Using Equation 24, we make a direct comparison between the measured (Thomson scattering) p_u , the maximum upstream pressure limit $p_{u,crit}$ and $p_{t,crit}$ (which, in the case of no momentum loss – $f_{mom} = 1$, equals $p_{u,crit}$) as a function of time (Figure 15e). The measured upstream pressure rises during the density ramp, while $p_{u,crit,fmom}$ and $p_{t,crit}$ drop due to a decrease in q_{recl} and p_u crosses $p_{t,crit}$ and $p_{u,crit}$ at ~ 0.8 s, the detachment threshold. After that time the target pressure limit decreases further while volumetric momentum losses start to result in a bifurcation between the upstream/target critical pressures. Despite this bifurcation, $p_{u,crit}$ flattens and eventually rolls over, while p_u continues to track $p_{u,crit}$. This indicates that, even when considering the amount of observed momentum loss, the observed saturation/roll-over of the upstream pressure is *consistent* with the model.

Detachment requires target pressure loss (eq. 2) which could be engendered by volumetric momentum loss and/or upstream pressure loss. Our experimental measurements and analysis using the 2PMR (above) imply, given the amount of volumetric momentum loss, a saturation/reduction of the upstream pressure is required as well to reach $p_{t,crit}$, which is consistent with the *measured* reduction of the upstream pressure. However, this *consistency* does not indicate *causation*: e.g. it does not show that inadequate momentum loss on a given flux tube *causes* the upstream pressure to drop. As suggested earlier, other processes, i.e. upstream or divertor cross-field transport (particles and/or momentum), may be affecting the upstream pressure as well.

A commonly held assumption is that the upstream pressure remains constant/unaffected by detachment. That assumption results in the (mis)understanding that *all* the required p_t drop *must* be provided by *only* volumetric momentum losses. These TCV results, however, show that *both* an upstream pressure drop and volumetric momentum losses contribute to the required p_t drop. Accounting for upstream pressure changes is thus crucial for understanding detachment.

4.2.5 The role of momentum loss and upstream pressure loss in target ion current loss

As described in the introduction, researchers generally look at detachment with different emphases: power/particle balance and momentum balance, which mostly focusses on volumetric momentum losses. Both viewpoints for describing detachment must be consistent with Equation 2. As explained earlier, the 2PMR, which combines both points of view, predicts detachment occurs when power limitation starts ($P_{ion} \sim \frac{1}{2} P_{recl}$; $T_t \sim E_{ion}/\gamma \sim 4-6$ eV), which corresponds to the point where the ion target current increases slower than $1/T_t^{0.5}$, hence *requiring* a target pressure loss. Thus, both target pressure loss and power limitation are required for detachment when the divertor is the primary source of ions. For a demonstration of the equivalence of pressure and power balance points of view we refer the reader to Equation 21a & b, which was derived in the appendix as Equation A.8. which shows the 2PMR can be seen from either a power/particle or pressure balance description – which are equivalent in this model.

It is striking that the temperatures ($T_t < E_{ion}/\gamma \sim 4-6$ eV) at which target pressure loss *must* occur (2PMR), according to divertor-physics, corresponds to the temperatures at which volumetric momentum loss *can* occur, according to atomic physics. This seeming coincidence of plasma and atomic physics implies volumetric momentum loss develops when power ‘limitation’ conditions

($P_{\text{recl}} < 2P_{\text{ion}}$) are reached, implying that power ‘limitation’ is a requirement for detachment for both points of view discussed.

The results of Section 4.2.4 show that the commonly held assumption that the upstream pressure remains constant/unaffected by detachment is not always true. Instead, the upstream target pressure and any volumetric momentum loss must be consistent with each other. This means the role of volumetric momentum loss can only be fully understood if all the processes influencing the upstream pressure are understood. These may be divertor, scrape-off layer and core processes. Examples could include changes in cross-field transport of energy, momentum and particles or volumetric losses within a flux tube, or both. The reality, however, is that we lack a quantitative understanding of how p_u is influenced by both the core and divertor plasma, which likely requires an integrated core-edge model. Lacking such a model prevents us from fully ascertaining the role momentum loss plays in detachment.

Nevertheless, it is unlikely that momentum losses directly reduces the ion target current during fully power-limited ($P_{\text{recl}} \sim P_{\text{ion}}$) detachment as $I_t \sim P_{\text{recl}}/E_{\text{ion}}$ (section 4.1) for those conditions: momentum losses slow down the fluid velocity in a flux tube, but do not directly reduce the ion flux through the tube. Momentum losses may, however facilitate detachment indirectly by allowing higher upstream pressures, leading to higher divertor densities (for the same T_e) and thus higher divertor radiation and higher recombination rates.

4.3 Investigating additional ion sources and sinks

Although the ionisation source and the volumetric recombination sink within the divertor are sufficient to explain, within uncertainties, the target ion flux trend (section 3.2), additional ion sources and sinks may remain significant.

4.3.1 Contribution due to flows from the SOL into the outer divertor

In this work we have assumed that ion sources outside the divertor, leading to ion flows into the divertor (I_{up}), can be neglected as a source of ions reaching the target. While direct measurements of ion flows into the divertor are unavailable, we can estimate such flows through Equation 26, in which M_u is the upstream Mach number and r the radial distance from the separatrix [70], which includes fluid flows along the magnetic field but ignores several types of drift flows such as ExB flows. Furthermore, this investigation ignores the influence of ionisation upstream of the divertor.

$$I_{\text{up}} \approx 2 \pi M_u \frac{B_p}{B_t} \int_{\text{separatrix}}^{\text{wall}} r n_u(r) \sqrt{\frac{T_u(r)}{m_i}} dr \quad (26)$$

To estimate the *maximum* possible I_{up} , we use $M_u \sim 0.5$, the upper bound of a previous survey of upstream Mach number profiles across three tokamaks [70]. To compute this conservatively large I_{up} (Equation 26), separatrix upstream densities and temperatures were measured using Thomson scattering, while their profiles were measured with a reciprocating probe (details are provided in appendix A.2). The resulting I_{up} , shown in Figure 16 for the high current density ramp discharge previously discussed in sections 3 and 4.1, 4.2, increases during the core density ramp which, of course, also raise the SOL density and thus I_{up} . I_{up} remains small compared to the divertor source of ions and the target ion current except at the end pulse when recombination starts to become significant and the target current has rolled over. During detachment, I_{up} increases to $\sim 30\%$ of the ion (outer) target flux and ion source.

The overall particle balance (Equation 27) would be consistent with the addition of our estimated I_{up} within uncertainties. Even with I_{up} included, the ion source, I_i , remains the largest contributor to the

target ion flux and its roll-over after the detachment onset. Based on the measurements shown in section 3.1; it is likely that this is the case also for lower current (e.g. lower density) discharges.

$$I_t = I_{up} + I_i - I_r \quad (27)$$

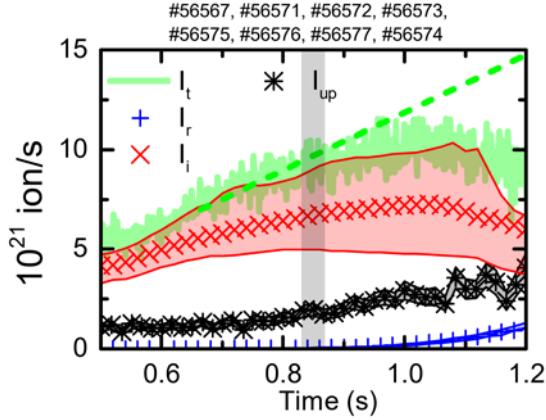


Figure 16: The target ion flux compared to the ion source, inferred ion flow from the SOL and the recombination rate.

delivered by the divertor ion source (e.g. ‘high recycling’), which is verified in this paper for TCV. The assumption that the divertor is in a high-recycling condition is more likely true for closed, higher density, divertors than for open divertors such as TCV.

A second question regarding the wider applicability of the TCV results is on the timing (and magnitude) of the significant contribution of the electron-ion recombination sink, which in TCV, is both after the detachment onset ($P_{ion}/P_{recl} \sim 0.5$; $T_t \sim 4-7$ eV) and the target ion current roll-over ($P_{ion}/P_{recl} \sim 0.7$; $T_t \sim 2$ eV). Instead, volumetric recombination becomes significant at temperatures < 1 eV, which occurs when $P_{ion} \sim P_{recl}$. Therefore, it seems that power limitation and the detachment onset ($P_{ion}/P_{recl} \sim 0.5$) occur *before* volumetric recombination becomes significant, which is expected to be general even to higher density machines as the argument based on temperature. ‘Power limitation’ ($q_{recl}/(E_{ion} \Gamma_t) < 2$) thus appears to be a universal requirement to reach the conditions for limiting the ion source and for lowering the target temperature to reach conditions for significant volumetric momentum loss and then finally, recombination.

However, how ‘quickly’ one goes from $P_{ion}/P_{recl} \sim 0.5$ to $P_{ion}/P_{recl} \sim 1$ (and thus recombination relevant conditions) during detachment can depend on a range of parameters and is likely better addressed in fluid models of higher density plasmas. When $P_{ion}/P_{recl} \sim 1$ conditions are achieved, the importance of volumetric recombination on TCV is significantly smaller than in higher density devices, such as C-Mod where volumetric recombination can drop the ion target flux by a factor 10-100 during a core density ramp [7]. This could also result in a more significant movement of the recombination and density peaks (front) at the deepest detached conditions.

We note that the effect of N_2 -seeding to reach detachment strongly reduces the level and importance of recombination as an ion sink for TCV. This does appear to scale to higher density tokamaks, such as C-Mod [7]. It thus seems generally true that volumetric recombination is not a requirement for (roll-over) detachment.

We do expect the characteristic gradient scale lengths of various quantities such as ionization, recombination and CX to be shorter (poloidal and along B) in tokamaks with higher densities and parallel power densities than for TCV. Certainly the parallel heat flux would be 100x larger in ITER than

4.4 Applicability of TCV results to other existing and planned tokamaks

A central focus of this paper is on the development of target ion current loss in detachment which is set in motion when the power flowing into the recycling region drops to twice the level required for the ion source - $q_{recl}/(E_{ion} \Gamma_t) \sim 2$, which leads to a ‘power limitation’ of the ion source. This appears to be the main driver of the I_t roll-over on TCV, while recombination has a much smaller effect and occurs after the roll-over of I_t . Power limitation can play a dominant role in ion current loss during detachment when I_t is (almost) fully

TCV leading to smaller parallel-to-B temperature scale lengths in absolute value and relative to the divertor size $\Delta L_{q\parallel}$ ($\Delta L_{q\parallel} \sim \Delta T / q_{\parallel}$ where ΔT is set by the impurity cooling curve, ~ 10 s of eV for carbon) [71]; this would lead to more localized impurity radiation and ionisation regions than in TCV. In addition, higher density will lead to shorter CX and ionization mean free paths. The ions and neutrals will be better equilibrated reducing the transfer of momentum per each CX occurrence. Such higher divertor densities, for the same upstream conditions, may be facilitated by the planned baffle upgrade [72] of TCV.

There is another likely key change in divertor characteristics engendered by larger P_{sep} and q_{\parallel} . Intrinsic carbon radiation in TCV suffices to lower q_{recl} so that it limits the ionization source during density ramp discharges. However, as q_{\parallel} is increased, reaching $P_{\text{recl}} \sim 2 \times P_{\text{ion}}$ without additional impurity seeding is correspondingly more difficult to accomplish during density ramps only [73]. That is particularly true for operation with high-Z metallic walls where we expect less intrinsic divertor radiation, adding impetus to needing seeded impurities to detach. However, given that impurity seeded TCV plasmas clearly show lower volumetric recombination (also true for JET [34] and C-Mod [7]) than for density ramp-driven detachment, the connection between seeding and recombination needs to be better understood.

5. Summary

Spectroscopic measurements of the TCV outer divertor plasma, combined with novel analysis techniques, has enabled an in-depth study of the roles of various processes (ion and power sources and sinks) controlling the divertor target ion current during detachment. Of particular importance to this study is the new ability to determine the poloidal divertor ionization source profile, and thus the total divertor ion source. These novel measurements provide the *first experimental verification that the ion source (I_t) in the divertor is the primary determinant of the target ion current (I_t) from attached conditions through the detachment onset and I_t drop (roll-over) in TCV*. The volumetric electron-ion recombination ion sink is relatively small or negligible until after I_t roll-over when T_t reaches low values. *Volumetric recombination thus seems not to be a requirement for detachment and only occurs after roll-over.*

Our power balance measurements during a core density ramp show that the onset of detachment occurs at a point when the power flowing into the divertor minus divertor impurity radiation (the power flowing into the recycling region), P_{recl} , drops to a value that is twice P_{ion} , the measured power required for ionization ($f_{\text{ion}} \equiv P_{\text{recl}} / P_{\text{ion}} \sim 2$). At that point the target temperature $T_t \sim 4\text{--}7$ eV and the target ion current deviates from the expected attached scaling (linearly with upstream density on TCV). As $P_{\text{recl}} / P_{\text{ion}}$ and T_t continue to drop during a core density scan, the ion source and target ion current start dropping (roll-over) at $P_{\text{recl}} / P_{\text{ion}} \sim 1.4$ ($T_t \sim 2$ eV). As $P_{\text{recl}} / P_{\text{ion}}$ approaches 1, where little thermal/kinetic power reaches the target ($T_t \leq 1$ eV), the ion-electron recombination sink for ions can become significant, but only after I_t roll-over. *The above sequence, as well as power reduction to the ionization and target regions driving the detachment process, appear general beyond TCV*. Essentially the same sequence is followed when using impurity seeding to reach detachment where we find that the role of recombination is further diminished.

We have also shown that our experimental measurements are consistent with analytic and 2D modelling predictions. *Simple power and particle balance analytic models, using target temperature measurements, predict the target ion current from attached through detachment onset and the current roll-over in quantitative agreement with the I_t measurement*. It also shows that the ion source can be written as a trade-off between the maximum possible ion source ($P_{\text{recl}} / E_{\text{ion}}$) and fraction of that

power spent on ionisation ($f_{\text{ion}} = P_{\text{ion}}/P_{\text{recl}}$), which increases with decreasing T_t/E_{ion} . The f_{ion} predicted from T_t/E_{ion} quantitatively agrees with f_{ion} obtained directly from spectroscopic measurements.

However, the ion source prediction from power and particle balance must also be consistent with the sheath conditions ($p_t \propto \Gamma_t T_t^{1/2}$) – as is done in the ‘2PMR’ model in this work. That consistency leads to three equivalent quantitative predictions for the detachment onset: $T_t = E_{\text{ion}}/\gamma \sim 4\text{--}7$ eV, $f_{\text{ion}} = 0.5$, and $p_t/q_{\text{recl}} = \sqrt{\frac{m_i}{2E_{\text{ion}}\gamma}} \sim 8$ N/MW. *All three have been found to match, within uncertainties, the experimentally-determined detachment onset.* The extension of the I_t prediction beyond these thresholds *requires* pressure loss. The observation that *atomic physics* supplies volumetric momentum losses when the detachment onset criteria requires it (when required by plasma physics) is striking.

Our measurements have further validated the physics included in the SOLPS modelling code. *Measured outer divertor poloidal profiles of ion/power sources, sinks and other plasma parameters are compared with SOLPS predictions for three points in the detachment process with generally good quantitative agreement.*

Several caveats have emerged from this study: First, the linear increase of the target ion flux with upstream density for an attached divertor is consistent with taking into account all aspects of the 2PMR model. This points out that the often-used degree of detachment (DoD) scaling ($\Gamma_t \propto \bar{n}_e^{-2}$) must be modified to account for changes in upstream parameters (n_e , T_e) and divertor radiation. Lastly, target pressure loss during detachment can be due to both volumetric momentum losses and a drop in the upstream pressure; it is unclear whether the upstream pressure loss is driven by upstream processes (e.g. cross-field transport) or by changes in the divertor, or both.

Acknowledgments

The authors would like to thank S. Krasheninnikov, D. Moulton and P. Stangeby, for discussions of the physics processes, previous work and spectroscopic techniques relevant to this paper. This work has been carried out within the framework of the EUROfusion Consortium and has received funding from the Euratom research and training programme 2014–2018 under Grant Agreement No. 633053. The views and opinions expressed herein do not necessarily reflect those of the European Commission. This work was supported in part by the Swiss National Science Foundation. The PhD research of K. Verhaegh was supported by funding from the University of York and the Swiss National Science Foundation. B. Lipschultz was funded in part by the Wolfson Foundation and UK Royal Society through a Royal Society Wolfson Research Merit Award as well as by the RCUK Energy Programme (EPSRC grant number EP/I501045).

A.1 Two point model with recycling energy losses (2PMR)

In literature [4, 10], the effect of recycling losses has been added to the Two Point model [4], which we refer to as the “2PMR”. In this section, a more explicit derivation of adding the effect of recycling energy losses to the Two Point model is provided; which has been utilised for several predictions in section 4.2. This 2PMR model provides both a prediction for the ion target current trend, the target temperature and a quantitative criterion for the expected onset of detachment. A more detailed discussion on this ‘2PMR’ can be found in [36].

A.1.1 2PMR derivation

Recycling energy losses have been included in the Two Point model by assuming that the target ion flux (Γ_t), on a single flux tube, is fully determined by the ionisation source on that particular flux tube (Γ_i) (Equation A.1). As such, it is assumed that both ion flows from outside of the ionisation region

towards the target and recombination in the divertor are negligible. Furthermore, cross-field transport of heat and/or particles is ignored.

$$\Gamma_t = \Gamma_i \quad (\text{A.1})$$

It is further assumed that the power flux entering the recycling region (q_{recl}) equals the kinetic part of the heat flux reaching the target $q_t = \gamma \Gamma_i T_t$ plus the power flux spent on ionisation $E_{ion} \Gamma_i$, yielding a relation relating q_{recl} to q_t , and T_t^* which is defined as the ratio between energy spent on ionisation and kinetic energy reaching the target $T_t^* = \frac{\gamma T_t}{E_{ion}}$, as explained in section 4.1.

$$\begin{aligned} q_{recl} &= E_{ion} \Gamma_i + q_t = \gamma \Gamma_i T_t \left(1 + \frac{E_{ion}}{\gamma T_t} \right) \\ \rightarrow q_t &= q_{recl} \frac{T_t^*}{1+T_t^*} = q_{recl} f_{kin} \end{aligned} \quad (\text{A.2})$$

Using the sheath target ion flux (Equation A.3), a relation for the target temperature as function of the heat flux reaching the target and the target pressure p_t can be established (note that p_t is the total target pressure); which is similar to the “basic” two point model result [4]. Here it is assumed that the Mach velocity near the target is 1.

$$\begin{aligned} q_t &= \gamma n_t k T_t \sqrt{\frac{2 T_t}{m_i}} \\ \rightarrow T_t &= \frac{2 m_i}{\gamma^2} \left(\frac{q_t}{p_t} \right)^2 \end{aligned} \quad (\text{A.3})$$

By combining Equation A.3 with Equation A.2 a prediction for T_t is obtained (Equation A.4), which is the central equation of the 2PMR.

$$T_t = \frac{2 m_i}{\gamma^2} \left(\frac{q_{recl}}{p_t} \right)^2 \left(\frac{\gamma T_t}{\gamma T_t + E_{ion}} \right)^2 \quad (\text{A.4})$$

Equation A.4 can be solved either numerically or, under the assumption that p_t , q_{recl} , E_{ion} are all fixed parameters (e.g. if they do not have a T_t dependence apart from Equation A.4), Equation A.4 can be re-written as a quadratic equation, yielding an analytic expression for T_t – Equation A.5. That assumption implies that p_t does not drop as T_t is decreased, which is required for a simultaneous reduction of the ion target current and the target temperature – e.g. detachment. First we discuss the expected solutions making the assumption that p_t is fixed, while we discuss the implications of p_t having to drop during detachment later.

$$\begin{aligned} T_t^2 + \left(\frac{2 E_{ion}}{\gamma} - \frac{2 m_i}{\gamma^2} \left(\frac{q_{recl}}{p_t} \right)^2 \right) T_t + \frac{E_{ion}^2}{\gamma^2} &= 0 \\ T_t &= \left(\frac{m_i}{\gamma^2} \left(\frac{q_{recl}}{p_t} \right)^2 - \frac{E_{ion}}{\gamma} \right) \pm \sqrt{\frac{m_i}{\gamma^2} \left(\frac{q_{recl}}{p_t} \right)^2 - \frac{2 E_{ion}}{\gamma}} \end{aligned} \quad (\text{A.5})$$

The quadratic equation for T_t has two solutions (Equation A.5), of which only the positive branch ($T_t \geq \frac{E_{ion}}{\gamma}$) is stable (Equation A.8) as has been explained in literature [4, 9, 10]. Hence, we assume that the negative branch, $T_t \leq \frac{E_{ion}}{\gamma}$, of Equation A.5 cannot occur.

Combining Equation A.2 and Equation A.5 (with no recombination) enables us to obtain a relation for the target ion flux in terms of p_u , q_{recl} , E_{ion} and physical constants, which can be used to predict Γ_t when $T_t \leq \frac{E_{ion}}{\gamma}$.

$$q_{recl} = E_{ion}\Gamma_t + q_t = \gamma\Gamma_t T_t \left(1 + \frac{E_{ion}}{\gamma T_t}\right)$$

$$\Gamma_t = \frac{q_{recl}}{\gamma T_t + E_{ion}} = \frac{q_{recl}}{\gamma \frac{2 m_i}{\gamma^2} \left(\frac{q_{recl}}{p_t}\right)^2 \left(\frac{\gamma T_t}{\gamma T_t + E_{ion}}\right)^2 E_{ion} + \gamma T_t}$$

$$\Gamma_t = \frac{\gamma p_t^2}{2 m_i q_{recl} f_{kin}(T_t)} \quad (A.6)$$

It is important to note that Equation A.6, which has a form equivalent to the ‘default’ Two Point model expected ion target current trend (e.g. $\Gamma_t = \frac{\gamma p_t^2}{2 m_i q_t}$), is identical to Equation A.7 which is essentially the flux surface’s equivalent of Equation 18 where the 2PMR provides the $f_{ion}(T_t, E_{ion})$ solution. Therefore, the 2PMR essentially provides a bridge between the model treated in section 4.1, based on only power and particle balance, and the ‘default’ Two Point model for divertor modelling.

$$q_{recl} = E_{ion}\Gamma_t + q_t = \gamma\Gamma_t T_t \left(1 + \frac{E_{ion}}{\gamma T_t}\right)$$

$$\Gamma_t = \frac{q_{recl}}{\gamma T_t + E_{ion}} = \frac{q_{recl}}{E_{ion}} \frac{E_{ion}}{E_{ion} + \gamma T_t}$$

$$\Gamma_t = \frac{q_{recl}}{E_{ion}} f_{ion}(T_t, E_{ion}) \quad (A.7)$$

For convenience, the expressions for $f_{kin}(T_t, E_{ion})$ and $f_{ion}(T_t, E_{ion})$ are provided in Equation A.8 and A.9 respectively.

$$f_{kin}(T_t) = \frac{\gamma T_t}{E_{ion} + \gamma T_t} = \frac{\frac{m_i}{\gamma} \left(\frac{q_{recl}}{p_t}\right)^2 + \sqrt{m_i} \left(\frac{q_{recl}}{p_t}\right) \sqrt{\frac{m_i}{\gamma^2} \left(\frac{q_{recl}}{p_t}\right)^{c^2} - \frac{2E_{ion}}{\gamma}} - E_{ion}}{\frac{m_i}{\gamma} \left(\frac{q_{recl}}{p_t}\right)^2 + \sqrt{m_i} \left(\frac{q_{recl}}{p_t}\right) \sqrt{\frac{m_i}{\gamma^2} \left(\frac{q_{recl}}{p_t}\right)^2 - \frac{2E_{ion}}{\gamma}}}$$

$$f_{kin}(T_t) = 1 - \frac{E_{ion}}{\frac{m_i}{\gamma} \left(\frac{q_{recl}}{p_t}\right)^2 + \sqrt{m_i} \left(\frac{q_{recl}}{p_t}\right) \sqrt{\frac{m_i}{\gamma^2} \left(\frac{q_{recl}}{p_t}\right)^2 - \frac{2E_{ion}}{\gamma}}} \quad (A.8)$$

$$f_{ion}(T_t) = \frac{E_{ion}}{E_{ion} + \gamma T_t} = \frac{E_{ion}}{\frac{m_i}{\gamma} \left(\frac{q_{recl}}{p_t}\right)^2 + \sqrt{m_i} \left(\frac{q_{recl}}{p_t}\right) \sqrt{\frac{m_i}{\gamma^2} \left(\frac{q_{recl}}{p_t}\right)^2 - \frac{2E_{ion}}{\gamma}}} \quad (A.9)$$

A.1.2 2PMR and detachment onset criteria

The ion current Equations A.8 and A.9 do not support an ion current roll-over when decreasing T_t , as decreases in q_{recl} (or increases in p_u) will lead to an increase in Γ_t due to the $f_{ion}(T_t, E_{ion})$ dependency; for the applicability regime for these Equations $T_{t,crit} > \left(\frac{E_{ion}}{\gamma}\right)$. Therefore, the derived 2PMR above only allows attached solutions – detached solutions would require target pressure loss.

Furthermore, as shown in expression A.5, there is also a lowest possible temperature in this model, provided by Equation A.10. The reason being that any further temperature reduction (and detachment) must be paired with target pressure loss. Reaching this lowest possible temperature thus

implies reaching a condition where target pressure loss *needs to start to occur*. More explicitly, Equation A.4 can be re-written as $p_t = \sqrt{2 \gamma m_i \frac{q_{recl}}{E_{ion}}} T_t^{-1/2} \frac{T_t}{T_t + E_{ion}}$, which has a maxima at the temperature provided by Equation A.10. The physics behind this can be understood by considering the target pressure to be set by a competition between the ion target current and the target temperature ($p_t \propto \Gamma_t T_t^{1/2}$ - Equation 2). However, power/particle balance dictates that the higher the ionisation source (and thus Γ_t), the lower the target temperature (Equation 13). Due to those trade-offs the target pressure is maximised at Equation A.10 (for a given q_{recl} , E_{ion}), and any further reduction of the target temperature (and detachment) requires target pressure loss.

$$T_{t,crit} = \left(\frac{E_{ion}}{\gamma} \right) \quad (A.10)$$

Because of this reasoning, we define reaching the condition of Equation A.10 as a criterion for the onset of detachment – similarly to Krasheninnikov [10], while Stangeby recognises it ([4] p. 238, [9]) as an applicability limit of the 2PMR without momentum (or target pressure) losses. It is important to note that in the 2PMR only the trend of the *target pressure counts*: e.g. it does not matter whether this is reduced due to volumetric momentum losses or due to upstream pressure loss.

There are two other equivalent criteria for reaching this critical target temperature. First, this point corresponds to $f_{ion} = f_{kin} = 0.5$, using Equation A.2; e.g. 50% of the power flux going into the recycling region is being used for ionisation – a new quantitative detachment criteria derived and emphasised in this work. A second, equivalent condition is a threshold in terms of p_t/q_{recl} as emphasised in [10], which can be written in terms of the target sound speed at the target temperature (Equation A.11).

That threshold is identical to the target pressure reaching the maximum: $(p_t)_{crit} = q_{recl} \sqrt{\frac{m_i}{2E_{ion}\gamma}}$.

Assuming no momentum losses occur, the target pressure p_t in previous Equations A.3 – A.11 can be replaced with the upstream pressure p_u , as is customary when using the Two Point model. This implies that the p_t/q_{recl} limit can be written as a p_u/q_{recl} limit [10, 14].

$$\begin{aligned} \frac{m_i}{e\gamma^2} \left(\frac{q_{recl}}{p_t} \right)^2 - \frac{2E_{ion}}{\gamma} &= 0 \\ \left(\frac{p_t}{q_{recl}} \right)_{crit} &= \sqrt{\frac{m_i}{2E_{ion}\gamma}} \\ \left(\frac{p_t}{q_{recl}} \right)_{crit} &= \frac{1}{\gamma c_{st} \left(T_t - \frac{E_{ion}}{\gamma} \right)} \end{aligned} \quad (A.11)^2$$

Since reaching the condition of equation A.11 means the target pressure is maximised, $\left(\frac{p_t}{q_{recl}} \right)_{crit} \leq \sqrt{\frac{m_i}{2E_{ion}\gamma}}$ must always be satisfied. This means that during detachment, the *minimum* target pressure loss after the onset of detachment while q_{recl} and E_{ion} vary is given by equation A.11. Combining equation A.11 with equation A.4 shows that, in the case of a *minimum* target pressure loss, the target

² This critical threshold (in the form p_u/q_{recl} – this will be explained later) is twice larger than in [9]. However, the calculated threshold (Figure 20C) is ~ 2 x smaller than the quoted 15 N/MW [9] likely due to different values used for E_{ion} , γ . However, this point is identical to the $p_u^2 / q_{||}$ reached in [4,8], using Equations 5.37, 5.39 on p. 237, 238 with $T_t = E_{ion} / \gamma$.

temperature will remain fixed at $\frac{E_{ion}}{\gamma}$ and thus f_{ion} will remain fixed at 1/2. The ion target current can, however, drop when q_{recl} is lowered or E_{ion} is increased.

Target temperatures lower than $\frac{E_{ion}}{\gamma}$ can be accessed by specifying that the target pressure *reduces as function of* T_t . This dependency requires solving Equation A.4 numerically and, if the specified $p_t(T_t)$ reduction is a sufficiently strong function of T_t , can lead to T_t below the previous quoted maxima. This is, for instance, achieved by assuming that the upstream pressure is constant while specifying a specific momentum loss $f_{mom} \equiv p_t/p_u$ as function of T_t , as is done in [9], which cause a bifurcation between p_t and p_u . Such relations alter the solution structure of Equation A.4 in such a way that no longer a quadratic solution (Equation A.5) is obtained – and thus no longer a stable high temperature / unstable low temperature branch for T_t exists – instead one stable solution exists. This agrees with 1D simulations which indicated that enabling volumetric momentum losses lead to a more stable detachment behaviour [60]. More information of the dynamics of the 2PMR in the $T_t < \frac{E_{ion}}{\gamma}$ regime can be found in [9, 36].

Although including a specific $p_t(T_t)$ enables one smooth solution without a critical point, throughout this solution the target pressure must remain below the maximum target pressure quoted previously. Therefore, dependent upon the amount of momentum losses f_{mom} , there is also a maximum possible upstream pressure, indicated by Equation A.12.

$$\left(\frac{p_u}{q_{recl}}\right)_{crit} = \frac{1}{f_{mom}\gamma c_{st}(T_t = \frac{E_{ion}}{\gamma})} \quad (A.12)$$

A.2 Evaluating and applying the 2PMR model with experimental data

First, we aim to predict the *detachment onset for the flux surface corresponding to the separatrix*. This means that p_u , E_{ion} and q_{recl} should correspond to their separatrix values, which is straightforward for p_u (obtained by Thomson scattering from the chord closest to the separatrix). However, assumptions must be made to estimate E_{ion} and q_{recl} on a particular flux surface.

As explained in sections 4.1.3 and [35], an estimate of E_{ion} is obtained from spectroscopic inferences, which provides an “effective” E_{ion} , which is divertor averaged over all the different flux surfaces. Such an assumption has a negligible effect on the 2PMR predicted detachment onset.

To estimate q_{recycl} at the separatrix we divide the power entering the ionisation region (P_{recycl} – section 3.3), with an effective area, $A_{eff} = 2\pi R_{target} \frac{B_t}{B_p} \lambda_{SOL}$ [4], where it is assumed that the radial location of the ionisation region is the same as the target radius. A_{eff} depends on the ratio between the toroidal and poloidal field ($\frac{B_t}{B_p}$) and a scrape-off-layer width λ_{SOL} . The SOL width has been approximated by using $\lambda_{q,int}$ of the heat flux profile measured through IR imaging at the target, which has been mapped upstream [41]. The choice for a characterisation using $\lambda_{q,int}$ for the spatial profile of q_{recycl} across flux surfaces has been made as this parametrisation is more robust during detached regimes than the Eich fit [41]. It is assumed that the spatial profile of q_{recl} is the same as that of the target heat flux, which enables extracting q_{recl} from P_{recl} using $\lambda_{q,int}$. Further discussion on this follows below. Uncertainties of the characterization of A_{eff} have been neglected and could lead to systematic deviations from the portrayed trend of q_{recycl} .

Instead of estimating the detachment onset, we also wish to apply this technique to model the behaviour of the integrated ion current as function of ‘upstream’ parameters (p_u , q_{recl}), which can be

compared with the experimentally measured integrated ion current. This requires Equation A.8 (or A.9) to be integrated along the entire divertor floor. For the sake of simplicity, we assume that f_{kin} at the separatrix is characteristic for the entire divertor – Equation A.19. Such an assumption can be made since we are interested in comparing ion current trends (as opposed to absolute values) and, in addition, the influence of f_{kin} on Equation A.8 is limited as f_{kin} can only vary between 0.5 and 1.

$$I_t = \int \Gamma_t$$

$$I_t \propto \frac{1}{f_{kin}} \int \frac{p_u^2}{q_{recl}} \quad (\text{A.19})$$

To simplify the expression of the integral, the upstream density and temperature profiles are broken up in their separatrix values (e.g. n_u^0) times a function describing their profile behaviour (e.g. $f_{n_u}(r)$) as shown in Equation A.20.

$$n_u(r) = f_{n_u}(r)n_u^0$$

$$T_u(r) = f_{T_u}(r)T_u^0$$

$$q_{recl}(r) = f_{q_{recl}}(r)q_{recl}^0 \quad (\text{A.20})$$

To maximize temporal resolution, the upstream separatrix density/temperature are obtained from Thomson scattering, while the normalised upstream density/temperature profiles ($f_{n_u}(r)$, $f_{T_u}(r)$) are obtained by fitting reciprocating probe upstream density/temperature profiles, at the probe plunge times, with a double exponential: $f_{n_u} = A_1 e^{-\frac{r-r_{sep}}{\lambda_1}} + A_2 e^{-\frac{r-r_{sep}}{\lambda_2}}$ where r_{sep} is the separatrix radius upstream. A single exponential profile using $\lambda_{q,int}$ has been used to describe the profile of $q_{recl}(r)$, whose integral equals P_{recl} , again assuming that the heat flux shape at the target is similar to the heat flux shape of q_{recl} upstream entering the recycling region. Volumetric radiation could, however, alter this heat flux shape. Nevertheless, if the impurity radiation region and the ionisation region are well separated most of the radiative dissipation would happen in the impurity radiation region upstream of both the target and the recycling region; making it more likely that the shapes of q_{recl} and the target heat flux are similar.

Using these profile expressions, the target ion flux can be expressed as shown in Equation A.14. The modelled integrated target ion current scales as $\frac{1}{f_{kin}}$ (evaluated at the separatrix – Equation A.10), times $\frac{p_u^2}{P_{recl}}$ (where p_u^0 is evaluated at the separatrix) times f_p , which is a parameter describing the influence of the evolution of all spatial profiles on I_t as indicated in Equation A.20, which is integrated from the separatrix until five times $\lambda_{q,int}$ away from the separatrix.

f_p outside of the reciprocating probe plunge times is interpolated by fitting a polynomial to f_p across all probe plunge times. Uncertainties in p_u^0 , P_{recl} and f_{kin} have been considered, while uncertainties in the profile description are neglected. The separatrix values of the upstream density/temperature/target temperature are referred to as n_u , T_u , T_t in the rest of the paper.

$$I_t \propto \frac{1}{f_{kin}} \times f_p \times \frac{p_u^2}{P_{recl}}$$

$$f_p = \int_{r_{sep}}^{\infty} \frac{f_{n_u}^2(r)f_{T_u}^2(r)}{f_{q_{recl}}(r)} dr \quad (\text{A.21})$$

References

1. Loarte, A., et al., *Chapter 4: Power and particle control*. Nuclear Fusion, 2007. **47**(6): p. S203-S263.
2. Reimold, F., et al., *Divertor studies in nitrogen induced completely detached H-modes in full tungsten ASDEX Upgrade*. Nuclear Fusion, 2015. **55**(3): p. 033004.
3. Pitcher, C.S. and P.C. Stangeby, *Experimental divertor physics*. Plasma Physics and Controlled Fusion, 1997. **39**(6): p. 779-930.
4. Stangeby, P., *The plasma boundary of magnetic fusion devices*. The Plasma Boundary of Magnetic Fusion Devices. Series: Series in Plasma Physics, ISBN: 978-0-7503-0559-4. Taylor & Francis, Edited by Peter Stangeby, vol. 7, 2000. **7**.
5. Matthews, G.F., *Plasma Detachment from Divertor Targets and Limiters*. Journal of Nuclear Materials, 1995. **220**: p. 104-116.
6. Loarte, A., et al., *Plasma detachment in JET Mark I divertor experiments*. Nuclear Fusion, 1998. **38**(3): p. 331-371.
7. Lipschultz, B., et al., *The role of particle sinks and sources in Alcator C-Mod detached divertor discharges*. Physics of Plasmas, 1999. **6**(5): p. 1907-1916.
8. Komm, M., et al. *Divertor Impurity Seeding Experiments at the COMPASS Tokamak*. in *27th IAEA Fusion Energy Conference (FEC 2018)*. 2018.
9. Stangeby, P.C., *Basic physical processes and reduced models for plasma detachment*. Plasma Physics and Controlled Fusion, 2018. **60**(4): p. 044022.
10. Krasheninnikov, S.I., A.S. Kukushkin, and A.A. Pshenov, *Divertor plasma detachment*. Physics of Plasmas, 2016. **23**(5): p. 055602.
11. Pshenov, A.A., A.S. Kukushkin, and S.I. Krasheninnikov, *Energy balance in plasma detachment*. Nuclear Materials and Energy, 2017. **12**: p. 948-952.
12. Kukushkin, A. and H. Pacher, *The role of “momentum removal” in divertor detachment*. Contributions to Plasma Physics, 2016. **56**(6 - 8): p. 711-716.

13. Kukushkin, A., H. Pacher, and R. Pitts, *Characteristics of divertor detachment for ITER conditions*. Journal of Nuclear Materials, 2015. **463**: p. 586-590.
14. Krasheninnikov, S.I. and A.S. Kukushkin, *Physics of ultimate detachment of a tokamak divertor plasma*. Journal of Plasma Physics, 2017. **83**(5): p. 155830501.
15. Post, D.E., *A Review of Recent Developments in Atomic Processes for Divertors and Edge Plasmas*. Journal of Nuclear Materials, 1995. **220**: p. 143-157.
16. Wising, F., et al., *Simulation of plasma flux detachment in Alcator C-Mod and ITER*. Journal of nuclear materials, 1997. **241**: p. 273-277.
17. Loarte, A., *Understanding the edge physics of divertor experiments by comparison of 2D edge code calculations and experimental measurements*. Journal of Nuclear Materials, 1997. **241-243**: p. 118-134.
18. Krasheninnikov, S., et al., *Plasma recombination and molecular effects in tokamak divertors and divertor simulators*. Physics of Plasmas, 1997. **4**(5): p. 1638-1646.
19. Borrass, K., R. Schneider, and R. Farengo, *A scrape-off layer based model for Hugill-Greenwald type density limits*. Nuclear fusion, 1997. **37**(4): p. 523.
20. Pitts, R.A., et al., *Divertor geometry effects on detachment in TCV*. Journal of Nuclear Materials, 2001. **290**: p. 940-946.
21. McCracken, G.M., et al., *Evidence for volume recombination in jet detached divertor plasmas*. Nuclear Fusion, 1998. **38**(4): p. 619-629.
22. Lumma, D., J.L. Terry, and B. Lipschultz, *Radiative and three-body recombination in the Alcator C-Mod divertor*. Physics of Plasmas, 1997. **4**(7): p. 2555-2566.
23. Terry, J.L., et al., *Volume recombination and opacity in Alcator C-Mod divertor plasmas*. Physics of Plasmas, 1998. **5**(5): p. 1759-1766.
24. Wenzel, U., et al., *Volume recombination in divertor I of ASDEX Upgrade*. Nuclear Fusion, 1999. **39**(7): p. 873.

25. Lipschultz, B., et al., *Ultrahigh densities and volume recombination inside the separatrix of the Alcator C-Mod tokamak*. Physical Review Letters, 1998. **81**(5): p. 1007-1010.
26. Terry, J.L., et al., *The experimental determination of the volume recombination rate in tokamak divertors*. Journal of Nuclear Materials, 1999. **266-269**: p. 30-36.
27. Verhaegh, K., et al., *Spectroscopic investigations of divertor detachment in TCV*. Nuclear Materials and Energy, 2017. **12**: p. 1112-1117.
28. Fil, A.M.D., et al., *Identification of the primary processes that lead to the drop in divertor target ion current at detachment in TCV*. Contributions to plasma physics, 2017.
29. Reimold, F., et al., *The high field side high density region in SOLPS-modeling of nitrogen-seeded H-modes in ASDEX Upgrade*. Nuclear Materials and Energy, 2017. **12**: p. 193-199.
30. Wischmeier, M., *Simulating divertor detachment in the TCV and JET tokamaks*. EPFL, 2005.
31. Pitts, R.A., et al., *Experimental investigation of the effects of neon injection in TCV*. Journal of Nuclear Materials, 1999. **266**: p. 648-653.
32. Monk, R.D., et al., *Interpretation of ion flux and electron temperature profiles at the JET divertor target during high recycling and detached discharges*. Journal of Nuclear Materials, 1997. **241-243**: p. 396-401.
33. Verhaegh, K., et al. *Spectroscopic investigation of ion sources/sinks during TCV detachment*. in *44th EPS Conference on Plasma Physics*. 2017. Belfast.
34. Lomanowski, B., et al., *Spectroscopic investigation of N₂ and Ne seeded induced detachment in JET ITER-like wall*. Nuclear Materials and Energy, 2018, submitted.
35. Verhaegh, K., et al., *Novel inferences of ionisation & recombination for particle/power balance during detached discharges using deuterium Balmer line spectroscopy*. 2019.
36. Verhaegh, K., *Spectroscopic Investigations of detachment on TCV, in Physics*. 2018, University of York: York.

37. Coda, S., et al., *Overview of the TCV tokamak program: scientific progress and facility upgrades*. Nuclear Fusion, 2017. **57**(10): p. 102011.
38. Février, O., et al., *Analysis of wall-embedded Langmuir probe signals in different conditions on the Tokamak à Configuration Variable*. Rev Sci Instrum, 2018. **89**(5): p. 053502.
39. Hawke, J., et al., *Improving spatial and spectral resolution of TCV Thomson scattering*. Journal of Instrumentation, 2017. **12**(12): p. C12005.
40. Boedo, J.A., et al., *Fast scanning probe for the NSTX spherical tokamak*. Rev Sci Instrum, 2009. **80**(12): p. 123506.
41. Maurizio, R., et al. *Divertor heat flux characterisation during detachment experiments in TCV*. European Plasma Physics (45th EPS) 2017; Available from: <http://ocs.ciemat.es/EPS2017PAP/pdf/P5.116.pdf>.
42. Bernert, M. *Analysis of the H-mode density limit in the ASDEX Upgrade tokamak using bolometry*. 2013; Available from: https://edoc.ub.uni-muenchen.de/16262/1/Bernert_Matthias.pdf.
43. Sheikh, U.A., et al., *A novel carbon coating technique for foil bolometers*. Rev Sci Instrum, 2016. **87**(11): p. 11D431.
44. Verhaegh, K., et al., *An improved understanding of the roles of atomic processes and power balance in divertor target ion current loss during detachment*. arXiv preprint arXiv:1810.04969, 2018.
45. Botev, Z.I., J.F. Grotowski, and D.P. Kroese, *Kernel density estimation via diffusion*. The Annals of Statistics, 2010. **38**(5): p. 2916-2957.
46. Bowman, C. *Applications of Bayesian Probability Theory in Fusion Data Analysis*. 2016; Available from: <http://etheses.whiterose.ac.uk/16978/>.
47. Cowles, M.K., *Applied Bayesian statistics: with R and OpenBUGS examples*. Vol. 98. 2013: Springer Science & Business Media.
48. OPEN-ADAS; *Open - Atomic Data Analysis Structure*. Available from: <http://http://open.adas.ac.uk/>.

49. Mullane, M.O. *Generalised Collisional Radiative data for hydrogen: ADAS Manual*. 2013; Available from: http://www.adas.ac.uk/notes/adas_c13-01.pdf.
50. Harrison, J.R., et al., *Detachment evolution on the TCV tokamak*. Nuclear Materials and Energy, 2017. **12**: p. 1071-1076.
51. Theiler, C., et al., *Results from recent detachment experiments in alternative divertor configurations on TCV*. Nuclear Fusion, 2017. **57**(7): p. 072008.
52. Reimerdes, H., et al., *TCV experiments towards the development of a plasma exhaust solution*. Nuclear Fusion, 2017. **57**(12): p. 126007.
53. Potzel, S., et al., *A new experimental classification of divertor detachment in ASDEX Upgrade*. Nuclear Fusion, 2014. **54**(1): p. 013001.
54. Lomanowski, B.A., et al., *Inferring divertor plasma properties from hydrogen Balmer and Paschen series spectroscopy in JET-ILW*. Nuclear Fusion, 2015. **55**(12): p. 123028.
55. Batishchev, O., et al., *Kinetic effects on particle and heat fluxes in detached plasmas*. Physics of Plasmas, 1996. **3**(9): p. 3386-3396.
56. Batishchev, O., et al., *Kinetic effects in tokamak scrape-off layer plasmas*. Physics of Plasmas, 1997. **4**(5): p. 1672-1680.
57. Rosato, J., Y. Marandet, and R. Stamm, *A new table of Balmer line shapes for the diagnostic of magnetic fusion plasmas*. Journal of Quantitative Spectroscopy and Radiative Transfer, 2017. **187**: p. 333-337.
58. Henderson, S.S., et al., *Determination of volumetric plasma parameters from spectroscopic N II and N III line ratio measurements in the ASDEX Upgrade divertor*. Nuclear Fusion, 2018. **58**(1): p. 016047.
59. Post, D., et al., *Calculations of energy losses due to atomic processes in tokamaks with applications to the International Thermonuclear Experimental Reactor divertor*. Physics of Plasmas, 1995. **2**(6): p. 2328-2336.

60. Dudson, B., et al., *The role of particle, energy and momentum losses in 1D simulations of divertor detachment*. arXiv preprint arXiv:1812.09402, 2018.
61. Togo, S., et al., *Effects of neutral particles on the stability of the detachment fronts in divertor plasmas*. Plasma and Fusion Research, 2013. **8**: p. 2403096-2403096.
62. Lipschultz, B., et al., *Divertor physics research on Alcator C-Mod*. Fusion Science and Technology, 2007. **51**(3): p. 369-389.
63. Niemczewski, A., et al., *Neutral particle dynamics in the Alcator C-Mod tokamak*. Nuclear Fusion, 1997. **37**(2): p. 151.
64. Février, O., et al. *Evolution of pressure drop during detachment in the TCV tokamak*. in *APS Conference Plasma Physics*. 2017. Milwaukee.
65. Pérez, I.P., et al., *SOL parallel momentum loss in ASDEX Upgrade and comparison with SOLPS*. Nuclear Materials and Energy, 2017. **12**: p. 181-186.
66. Moulton, D., et al., *Using SOLPS to confirm the importance of total flux expansion in Super-X divertors*. Plasma Physics and Controlled Fusion, 2017. **59**(6): p. 065011.
67. Pitcher, C., et al., *The role of friction in SOL pressure balance in Alcator C-Mod*. Journal of nuclear materials, 1999. **266**: p. 1009-1014.
68. Kotov, V. and D. Reiter, *Two-point analysis of the numerical modelling of detached divertor plasmas*. Plasma physics and controlled fusion, 2009. **51**(11): p. 115002.
69. Krasheninnikov, S.I., et al., *Stability of the detachment front in a tokamak divertor*. Journal of Nuclear Materials, 1999. **266-269**(Supplement C): p. 251-257.
70. Lipschultz, B., D. Whyte, and B. LaBombard, *Comparison of particle transport in the scrape-off layer plasmas of Alcator C-Mod and DIII-D*. Plasma Physics and Controlled Fusion, 2005. **47**(10): p. 1559-1578.
71. Lipschultz, B., F. L. Para, and I. Hutchinson, *Sensitivity of detachment extent to magnetic configuration and external parameters*. Nuclear Fusion, 2016. **56**(5): p. 056007.

72. Reimerdes, H., et al., *TCV divertor upgrade for alternative magnetic configurations*. **12**: p. 1106-1111-1106-1111.
73. Bernert, M., et al., *Power exhaust by SOL and pedestal radiation at ASDEX Upgrade and JET*. Nuclear Materials and Energy, 2017. **12**: p. 111-118.